Ceramics International 47 (2021) 30113–30128

Contents lists available at ScienceDirect

Ceramics International

journal homepage: www.elsevier.com/locate/ceramint

# Repair of spline shaft by laser-cladding coarse TiC reinforced Ni-based coating: Process, microstructure and properties

Liaoyuan Chen, Yu Zhao, Xin Chen, Tianbiao Yu *, Pengfei Xu

*School of Mechanical Engineering and Automation, Northeastern University, Shenyang, 110819, China*

ARTICLE INFO

*Keywords:*
Surface repair
Laser cladding
TiC
Composite coating
Microstructure
Mechanical properties

ABSTRACT

To repair the surface defects of spline shaft and improve wear resistance, the coarse TiC reinforced Ni-based composite coatings were fabricated on the spline shaft surface by laser cladding with six types of precursors containing Ni45, coarse TiC, and fine TiN powder. The effects of ceramic content and fine TiN addition on the formability, microstructure, and mechanical properties of the coatings were studied comprehensively. In TiC reinforced Ni-based coatings 1–3 without fine TiN addition, the porosity decreased from 20.415 % to 0.571 % with the increase of TiC concentration. The coatings mainly consist of CrB, Cr7C3, Cr23C6, coarse TiC, and γ-Ni. With the addition of fine TiN, the length of the ceramic phases in coatings 1#–3# decreased slightly, while volume fraction and porosity increased. Moreover, the ring-shaped Ti (C, N) phases were also detected at the edges of both undissolved TiC and TiN particles, which improved the bonding force between ceramics and matrix. Besides, these ceramics inhibited the generation of columnar crystals and eliminated the heat-affected zone. The performance test results show that the coating 3# with 30 wt% TiC and 6 wt% TiN exhibits the best wear resistance despite slightly decreased hardness, and its friction coefficient of 0.409 and wear rate of $42.44 \times 10^{-6}$ $mm^3$ $N^{-1} \cdot m^{-1}$ are, respectively, 0.667 and 0.307 times those of the substrate. Based on the additive/subtractive hybrid manufacturing technology, the optimized coatings were ground to obtain the finishing surface, which indicates that the coarse TiC reinforced coating can be employed in repairing the damaged parts.

## 1. Introduction

Spline shaft has exceptional properties including multi-tooth work, strong bearing capacity, shallow tooth root, and good alignment, thus it has been widely explored in aircraft, automobile, machine tool manufacturing, and general transmission as a type of key mechanical transmission parts. The spline shaft is often exposed to repeated cyclic friction and radial load under a harsh working environment, therefore, fatigue wear, pitting, or other defects are usually found on its surface, in particle, in the lack of lubrication and regular maintenance. Therefore, the scrap rate of the spline shaft is often higher than that of the commonly used shaft part [1,2]. Repairing the damaged spline shaft to prolong service life, rather than being replaced by another new one, is an economic and environmental-protection solution [3–5].

In recent decades, it has become an important research hotspot in the manufacturing industry to repair damaged parts by advanced additive manufacturing (AM) technology, such as coaxial or pre-powder laser cladding (LC), selective laser melting (SLM), direct metal deposition (DMD), tungsten insert gas (TIG) cladding, and so on [6–9]. To meet the specific requirements of dedicated parts, it is necessary to apply different precursor materials to repairing specific parts. Notably, the composition of the precursor material can be easily adjusted, and the scanning strategy is unlimited by the shape of the damaged metal parts [10,11], therefore, coaxial powder delivered LC or DMD shows unique advantages in the repairing process compared to other AM technologies [12,13]. Li et al. [14] studied the effect of groove shapes and scanning strategies on the bonding properties between the repaired zone and ductile cast substrate by LC Ni–Cu alloy coating. Results showed that cross scanning strategy could reduce thermal stress, and further restrain the crack during the solidification process. Oh et al. [15] achieved the repair of 316L stainless steel plate using the same material via DMD technology and found that repaired zones at a 0.5 mm groove depth showed no cracks and exhibited excellent metallurgical bonding with the substrate corresponding to the highest tensile strength of 709 MPa. To assess the feasibility of repairing Ti–6Al–4V and evaluate the mechanical properties of cladding material (deposit + substrate), Paydas

* Corresponding author. School of Mechanical engineering and Automation, Northeastern University, Shenyang, 110819, China.
*E-mail addresses:* chen1910113@163.com (L. Chen), zhaoyuneu@gmail.com (Y. Zhao), northeastern_cx@163.com (X. Chen), tianbiaoyudyx@gmail.com (T. Yu), xupengfei@me.neu.edu.cn (P. Xu).

https://doi.org/10.1016/j.ceramint.2021.07.189
Received 6 May 2021; Received in revised form 5 July 2021; Accepted 19 July 2021
Available online 24 July 2021

**Table 1**
Chemical compositions of Ni45 powder and 40Cr (wt%).

| Element | C | Cr | Mo | Si | Ni | Mn | B | Fe |
|---|---|---|---|---|---|---|---|---|
| Ni45 | 0.45 | 12.00 | – | 4.00 | Bal. | 0.10 | 2.40 | 10.00 |
| 40Cr | 0.37–0.44 | 0.80–1.10 | ≤0.10 | 0.17–0.37 | ≤0.30 | 0.50–0.80 | – | Bal. |

**Table 2**
The precursor powders for designed composite coatings (wt.%).

| Coating No. | Component content (wt.%) | | |
|---|---|---|---|
| | Ni45 | TiC | TiN |
| 0 | 100 | 0 | 0 |
| 1 | 90 | 10 | 0 |
| 1# | 88 | 10 | 2 |
| 2 | 80 | 20 | 0 |
| 2# | 76 | 20 | 4 |
| 3 | 70 | 30 | 0 |
| 3# | 64 | 30 | 6 |

et al. [16] applied different scanning strategies and deposition processes to fill the designed curved grooves present on the surface of titanium alloy. Results indicated that the repaired zones prepared by high/low incident energy both exhibited good metallurgical combination with the substrate and authors also pointed out that small porosity (<0.1 %) in the samples could be acceptable because the tensile properties were higher than those of the substrate. Koehler et al. [17] promoted repairing process via LC technology from the laboratory-scale to industrial application. The microhardness of the repaired zone of the crankshafts was about 450 HV, which was slightly higher than that of the substrate. In the study of the repairability of LC H13 steel material on damaged 45 steel gear by Zhu et al. [18], the hardness of the remanufactured zone was only 195 HV, which exhibited a great tendency to cause severe wear of the remanufactured tooth under the high speed and heavy load working conditions.

The above-mentioned literature reports clearly indicate that LC has been indicated as effective AM technology for repairing damaged metal parts. However, it was also found that the precursor for the repairing process is often a single alloy powder, thus the low hardness and poor wear resistance of the repaired zone do not easily meet the required mechanical properties, thus further reducing their service life. At the same time, many studies [19–22] indicated that the ceramics-reinforced metal matrix composite (MMC) coatings show high hardness and excellent wear resistance, which brings new opportunities for meeting the requirements of the mechanical properties for the repaired parts. Titanium carbide (TiC) ceramics with high hardness (about 3200 kg $mm^{-2}$), high melting point (3430 K), low coefficient of thermal expansion ($7.74 \times 10^{-6}$/K), and small enough density (4.93 g $cm^{-3}$) has been identified as an ideal candidate for a reinforcement phase in MMC coatings [23,24]. The generation of TiC phases in MMC coatings via LC technology can be divided into the following two ways: *in-situ* synthesized and directly added.

AlMangour et al. [25] added 8 vol% pure titanium (Ti) and 2 vol% graphite (C) particles to 316L powder and then melted the content with the laser beam. The *in-situ* TiC-reinforced Fe-based coatings were successfully fabricated on the AISI 304 austenitic steel. The results state that the volume fraction of the TiC phases is significantly affected by laser energy density. Muvvala et al. [26] pointed out that the shape of *in-situ* TiC in Inconel 718/TiC composite coating changed from small round to long needle-like with the increase of Ti + C component. When the content of Ti + C is more than 70 wt%, the cladding layer is defective, which makes it difficult to fabricate multi-tracks coatings for industrial applications. By comparing the content of TiC in the composite coatings prepared by *in-situ* synthesis and direct addition method using low-energy pulsed LC, Zhang et al. [27] found that only a small amount of Ti powder and graphite combined together to synthesize desired TiC, and the microhardness and wear resistance were also not significantly improved. Although the bonding properties between the *in-situ* formed ceramic phases and the matrix in the MMC coating were improved, two main limitations are encountered in the fabrication of MMC coating by the *in-situ* synthesis method. On the one hand, thermodynamic calculation and rapid solidification theory indicate that the temperature and element concentration fields are crucial for the preparation of *in-situ*

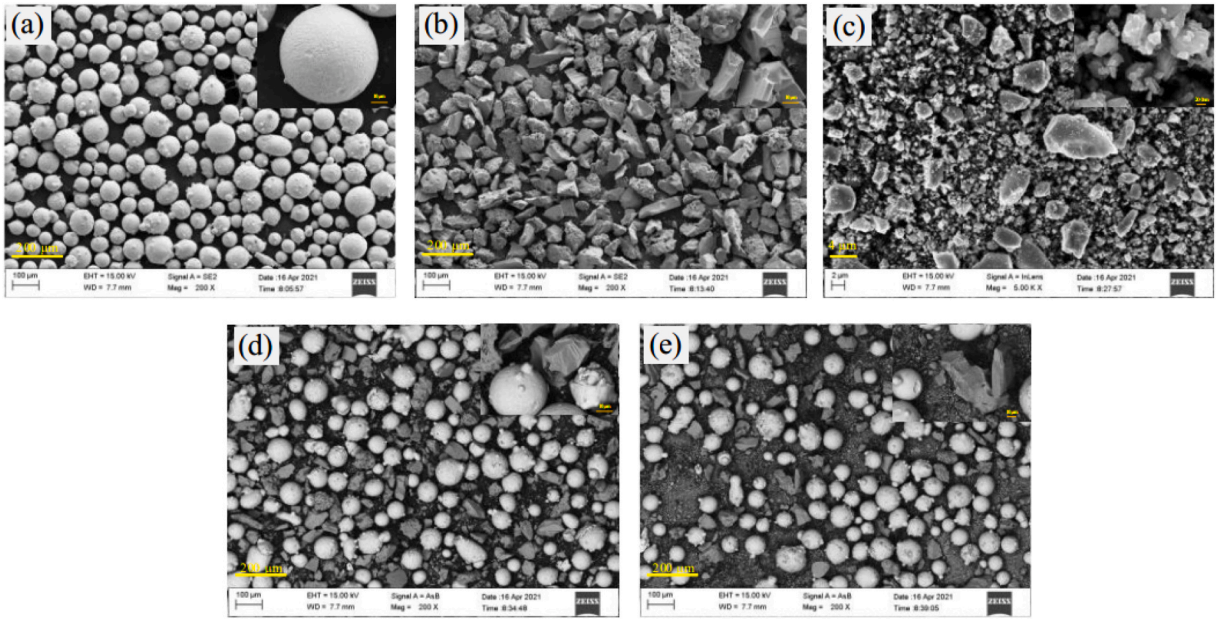


**Fig. 1.** SEM images of different precursor powders: (a) Ni45 powder, (b) TiC, (c) TiN, (d) Ni45 + 20 wt% TiC after ball milling, (e) Ni45 + 20 wt% TiC + 4 wt% TiN after ball milling.

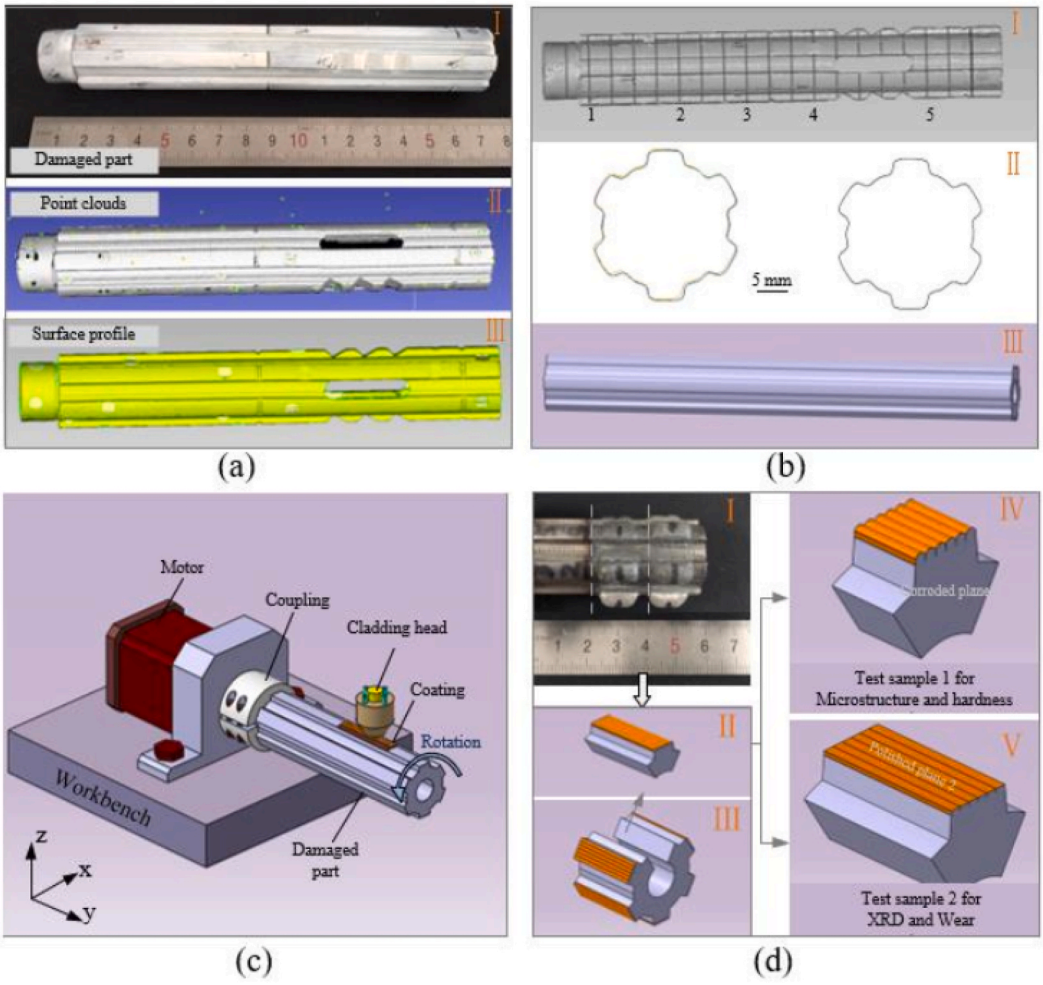


**Fig. 2.** (a) Obtained point clouds of the damaged part, (b) processing point cloud to obtain the 3D shape of the damaged part, (c) laser cladding process, (d) characterization of the repaired zone.

**Table 3**
The processing parameters for the repairing process.

| Power | Beam diameter | Scanning speed | Powder feed rate | Track space | Z-axis increment | Shielding gas |
|---|---|---|---|---|---|---|
| 425 | 1 mm | 4.5 mm/s | 0.85 r/min | 0.6 mm | 0.5 mm | Argon |

ceramics by LC [19,28]. At the same time, the short growth time of the hard phases could seriously limit their size after solidification [29–31], which is disadvantageous to further improve the wear resistance. On the other hand, in the process of LC, the size gradient between commercial alloy powder and additive in precursor makes it difficult for some small size additives into the molten pool, thus the volume fraction of the *in-situ* prepared ceramic phases is often lower than the designed value [27,29,32]. Compared to coating fabricated by the *in-situ* synthesis method, the coatings by direct injection method show a high ceramics volume fraction and large size [33,34], which is beneficial to improve the wear resistance of the composite coating. Previous studies [23,34,35] also found that the direct addition of TiC increased the crack sensitivity within the MMC coating. Reducing the scanning speed and preheating, and adding rare earth elements in the precursor powders can effectively reduce the cracks in the MMC coating [36,37]. Previous studies [30,38] have found that the Ti(C, N) demonstrates chemical stability and wear resistance, and the bonding strength between *in-situ* synthesized TiC and matrix is robust, which makes them difficult to peel off from the matrix during the wear process. Therefore, in this study, some fine TiN particles were added to the precursor powder, and Ti (C, N) phases were expected to be synthesized at the edge of coarse TiC particles.

Previous studies have shown that the fabrication process of TiC reinforced composite coating by LC is mature, and the hardness and wear resistance of the coating can be improved effectively. However, most of the works are to study the fundamental process and improve the performance of the composite coating. To the best of our knowledge, the combination of reverse engineering technology and additive/subtractive hybrid manufacturing technology to repair damaged metal parts has rarely been reported. In this study, the three-dimensional (3D) model of the damaged spline shaft with surface defects was constructed by reverse engineering technology. To evaluate the effect of the addition of coarse TiC on the formability, microstructure, and mechanical properties of the multi-tracks composite coating in detail, as a comprehensive study, six types of MMC coatings (two groups) were fabricated on the surface of the damaged spline shaft. Finally, the repair feasibility of TiC reinforced MMC coating on the damaged spline shaft surface was verified, and the finishing surface was also obtained. This study focuses on providing a technical reference for ceramic reinforced MMC coating in the surface repair of damaged parts, which is expected to further promote the industrial application of ceramic materials.

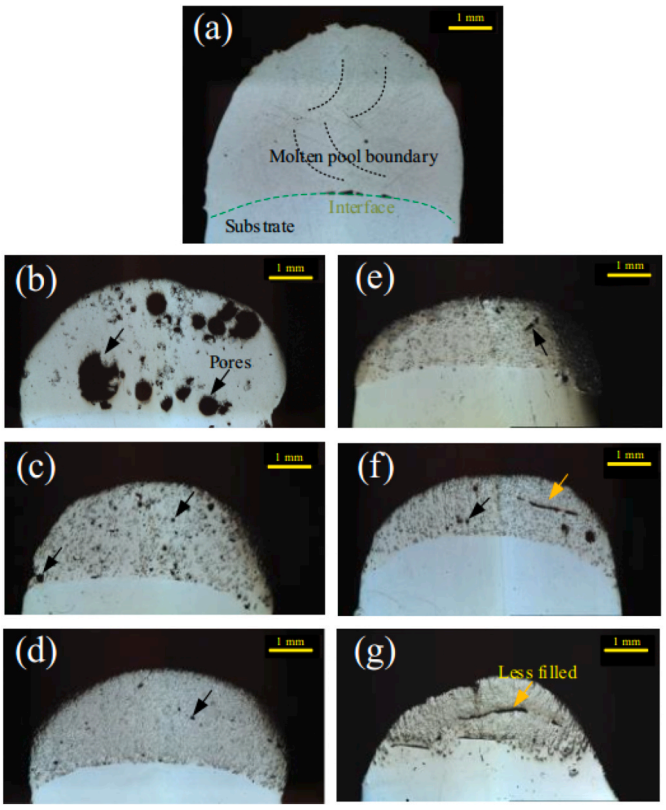


**Fig. 3.** Optical cross-sectional images of different coatings: (a) Ni45 coating, (b–d) coatings 1, 2, and 3, and (e–g) coatings 1#, 2#, and 3#.

## 2. Experimental

The precursor powder used in the experiment was mainly composed of commercial Ni45 powder (diameter: 69.08 μm), coarse TiC powder (purity 99.99 %, length: 78.31 μm), and fine TiN powder (purity 99.99 %, length: 1.77 μm). The material of the spline shaft is 40Cr steel (ISO, 41Cr4). Table 1 lists the elemental composition of the self-fluxing alloy Ni45 powder and 40Cr substrate. Coatings with different compositions were developed, and their compositions are presented in Table 2. Comparative analysis was carried out on coatings 1# to 3# to investigate the effect of fine TiN addition on the microstructure and mechanical properties of these coatings, respectively. To obtain homogeneous precursors, the composite powders were mixed in a planetary ball mill for 2 h, and the mass ratio of mixed media (alumina ball) to precursor was set as 2:1. The precursor powders were put in a constant temperature drying oven at 60 °C for 2 h to remove water vapor. The scanning electron microscopy (SEM) images of the original powders and mixed precursors 2 and 2# are shown in Fig. 1.

To analyze the repairability of different coatings on damaged parts and their microstructure and mechanical properties, the four operational steps were carried out, as shown in Fig. 2. Fig. 2(a) shows the process of obtained point cloud, and surface profile of the damaged part. Based on the principle of the service life unification of assembled parts, the size of the repaired parts should be consistent with that of the parts to be repaired, not with that of the new parts. The cross-sectional dimensions of five surface profiles were selected, and their average values were considered as the aimed cross-sectional dimensions of the damaged part. The 3D model of the damaged part is shown in Fig. 2(b)III. Fig. 2(c) represents the LC process. More details about the equipment can be found in our previous study [39]. After the preparation of one coating, the stepper motor was rotated 60° to adjust the position of the spline shaft, and then the next composite coating was built. The optimized process parameters are presented in Table 3. The morphology of the composite coatings on the spline shaft is shown in Fig. 2(d)I.

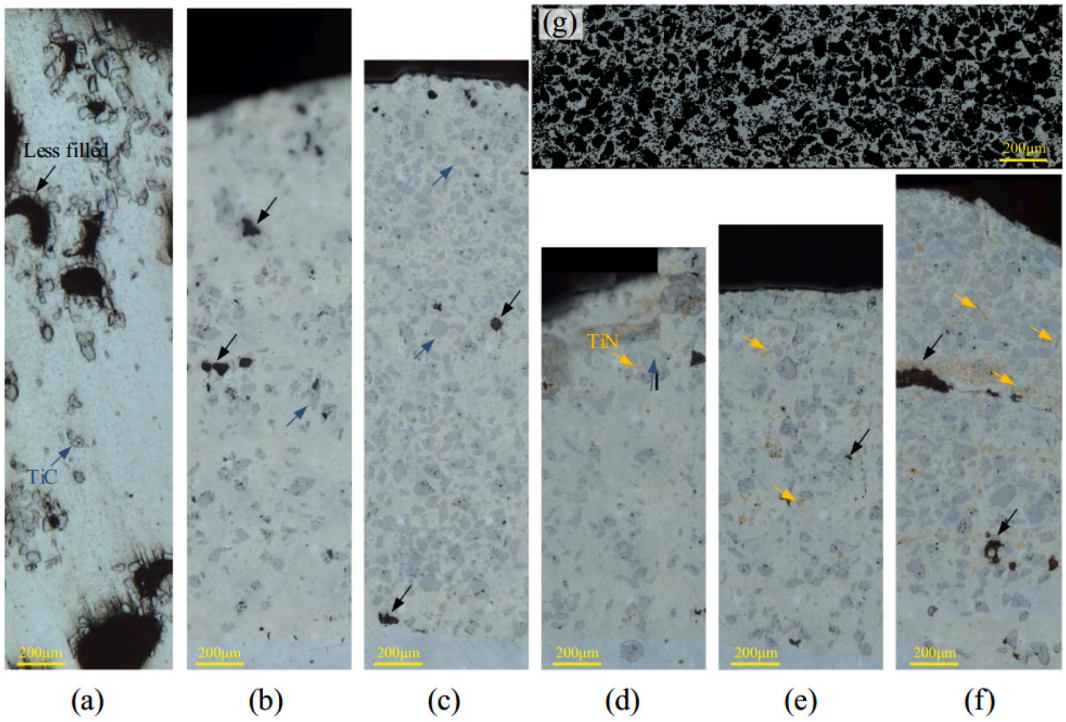


**Fig. 4.** Enlarged optical images showing the microstructure of different coating: (a–c) coatings 1, 2, and 3, (d–f) coatings 1#, 2#, and 3#, and (g) identified ceramic phases in coating 3.

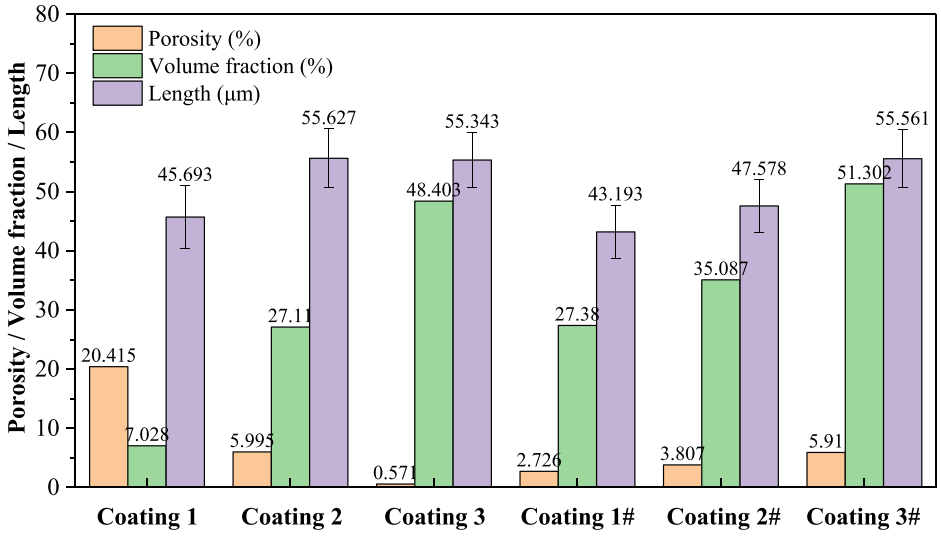


**Fig. 5.** Porosity, volume fraction, and length of TiC particles in each coating.

After fabrication, test samples were cut from the spline shaft. Plane 1 was ground, polished, ultrasonically cleaned in alcohol, and then corroded with aqua regia for 25–40 s. Cross-sectional morphologies and microstructure were investigated by laser confocal microscopy (OLS4000, Japan). X-ray diffraction (XRD, X Pertpro, Netherlands) with Cu-Kα radiation was used to analyze the phase composition of coatings. The morphologies of the phases were characterized by SEM (Zeiss, Germany) equipped with an energy dispersive spectroscopy (EDS) system. The Vickers micro-hardness of each coating was measured on the corroded plane 1 (shown in Fig. 2(d)) using an HV-1000 Vickers microhardness indenter along the growth direction under a load of 500g load and dwell time of 15 s. In order to analyze the wear resistance of the composite coatings, the linear reciprocating wear test was carried out on polished plane 2 using the material surface property tester (MFT-4000) with a φ4 mm zirconia ball with a hardness > 90 HRC as a counterpart, 15 N load, 5 mm linear track length, 220 mm $min^{-1}$ speed, and 60 min loading duration. The dimension of the test surface of each sample was 10 mm × 5 mm, and the Ra of the surface roughness was less than 0.03 μm. Each sample was tested three times. However, in case the two results were the same, the third experiment was not conducted. The coefficient of friction (COF) was automatically detected by its equipped software The 2D and 3D worn surfaces of composite coatings were also obtained by a laser confocal microscopy with the resolution of 0.12 and 0.01 μm in the horizontal and vertical direction, respectively.

## 3. Results and discussion

### 3.1. Formability

The cross-sectional morphologies of the composite coatings form an important basis for analyzing their deposition defects, the volume fraction, and the size of the ceramic phases. Fig. 3 illustrates the optical cross-sectional images of different coatings. Enlarged optical images and porosity, ceramic phases volume fraction and length of TiC particles in each coating are shown in Figs. 4 and 5, respectively. Fig. 3(b–d) and Fig. 5 demonstrate that the porosities in the coatings 1–3 decrease significantly with the increase of coarse TiC content. These trapped pores might be due to the failure of escape of CO or $CO_2$ gas generated by TiC oxidation from the molten pool during rapid solidification. On the one hand, the diffraction peak of TiNi was identified in the XRD pattern of coating 1. This indicates that the Ti element decomposed when TiC reacts with the Ni element in the molten pool to generate the intermetallic compound TiNi, while the residual C element reacts with oxygen in the air to form $CO_2$ or CO. On the other hand, the gas pores move in the molten pool under the action of the driving force of the molten pool. The large cross-sectional area often corresponds to a bigger bath size, which leads to an increase in the molten pool. The depth and life of the molten pool lead to the increase in the escape time of the gas pores in the molten pool, which increases the probability of the gas remaining in the solidified coating and eventually to larger porosity. Therefore, the cross-sectional area of the coating is positively related to the porosity (Fig. 3). A similar trend was observed in previous studies [40,41]. The increase of deposition speed is beneficial to reduce the porosity, but not to further increase the volume fraction of ceramic phases [36,42]. Comparative analysis of Fig. 3(b) and (e) indicate that the addition of 2 wt% TiN can effectively reduce the deposition defects, which can be attributed to the reduction of solidification time and the interaction mechanism between TiN and TiC. Previous studies [23,38] have shown that the [C] atom in TiC and [N] atom in TiN can replace each other to form a kind of ternary solid solution Ti(C, N) with excellent properties of both the components because they represent similar face-centered cubic crystal. Therefore, a large part of [C] atoms decomposed by coarse TiC could be dissolved into TiN, which reduced the concentration of the reactant that generated the gas. Therefore, the porosity of coatings 1#–3# decreased clearly.

Fig. 3(f) and (g) exhibit the existence of some less filled regions as well. The addition of fine TiC reduced the fluidity of the precursors (Fig. 1(e)), which resulted in flowing back of insufficient liquid metal to the bottom of the molten pool, and eventually formed deposition defects. Fig. 5 illustrates that the length of TiC in coating 1 is the smallest among all the coatings. This clearly states that the solubility of each TiC particle is the largest, which further promotes the generation of gas pores. Furthermore. Fig. 5 also display that the addition of fine TiN can increase the volume fraction of the ceramic phases and refine TiC particles.

### 3.2. Phase composition and morphologies

Fig. 6 shows the XRD results of each coating. The typical diffraction peaks of γ-Ni(Fe) solid solution, CrB, $Cr_7C_3$, and $Cr_{23}C_6$ are found in Ni45 coating, and these peaks are also detected by the previous studies [43,44]. When coarse TiC of varying contents was added to Ni45 alloy powder, some new diffraction peaks corresponding to reinforced phase TiC and intermetallic compound TiNi are also detected. At the beginning of LC, the decomposition of TiC led to the increase in the concentration of [Ti] and [C] atoms in the liquid metal, while [C] atoms reacted with

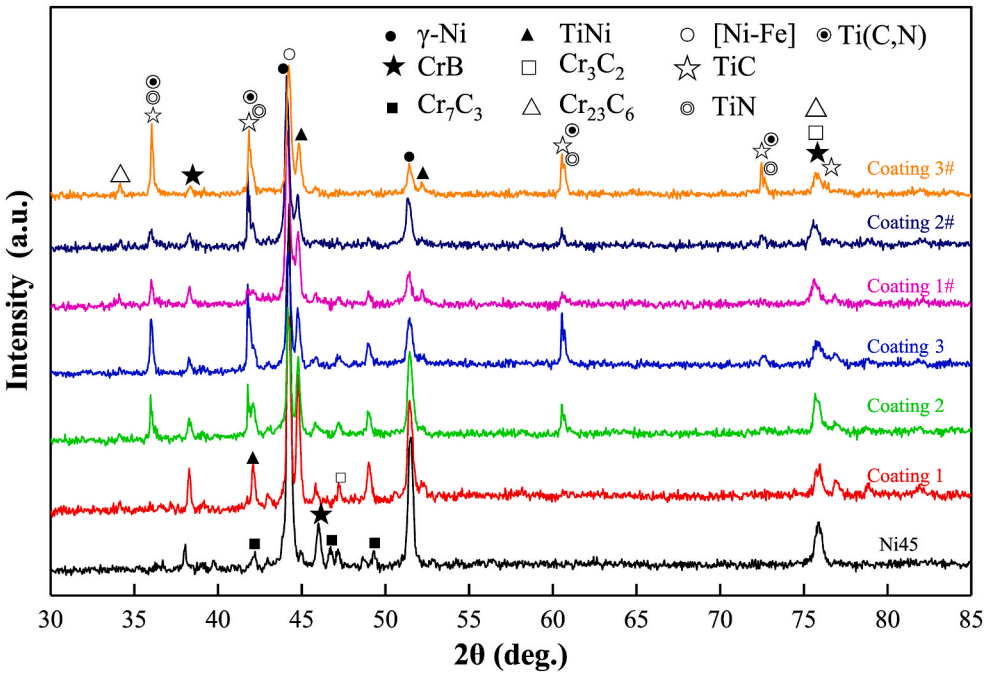


**Fig. 6.** XRD patterns of the different coatings with various TiC/TiN content.

oxygen in the air to form gas (Figs. 3b and 4a). During the solidification process, [Ti] atoms and rich [Ni] atoms combined together to synthesize TiNi rather than $Ti_2Ni$ at a lower Ti concentration compared to results presented by Liu et al. [19]. With the addition of fine TiN, the diffraction characteristics of the coatings 1#–3# changed compared to those of coatings 1–3. More than one diffraction peak is found near the diffraction peak of TiC, and the new peaks can be inferred as TiN and *in-situ* formed Ti(C, N). More remarkable, the diffraction intensity of each phase in the composite coating is lower than that of Ni45 coating, which indicates that the addition of ceramic particles is beneficial to refine the microstructure.

The EDS elemental analysis was carried out on coatings for in-depth investigation of the phase morphologies in detail. The EDS mapping analysis of Ni45 coating is shown in Fig. 7. Fig. 7(b) shows a back-scatter electron (BSE) image, exhibiting that the Ni45 coating mainly contains metal matrix (I), dark long strip structure (II), and gray cellular structure (III). Table 4 lists the EDS results of various phases marked for Ni45 coating, coating 2, and coating 2#. The metal matrix is proved to be rich in Ni and Fe elements. Analysis of XRD results indicates that the metal matrix consists of γ-Ni (Fe) solid solution, and Sun et al. [43] also detected the same results. Fig. 7(b) and (e) together reveal that the distribution of dark long strip structure (II), and cellular structure (III) matches exactly with that of the Cr element. In contrast, the B element mapping (Fig. 7(c)) can be matched to the long strip structure (II), which is darker than the cellular structure (III). However, C element mapping (Fig. 7(c)) exactly corresponds to the cellular structure (III). According to EDS results of P2–P5 presented in Table 4, the phases of II and III can be confirmed as Cr–B and Cr–C compounds, respectively.

Fig. 8 shows the surface distribution of Ti, B, Cr, C, Ni, Fe, Si elements in coating 2. Combined with the distribution of Ti and C elements (Fig. 8 (c) and f), and EDS results of P6 and P7 listed in Table 4, the shape of TiC in coating 2 could be roughly divided into three types, namely, original undissolved (UD) large-shaped, secondary precipitated small particle-like and cross-shaped. Noteworthy, the shape of secondary

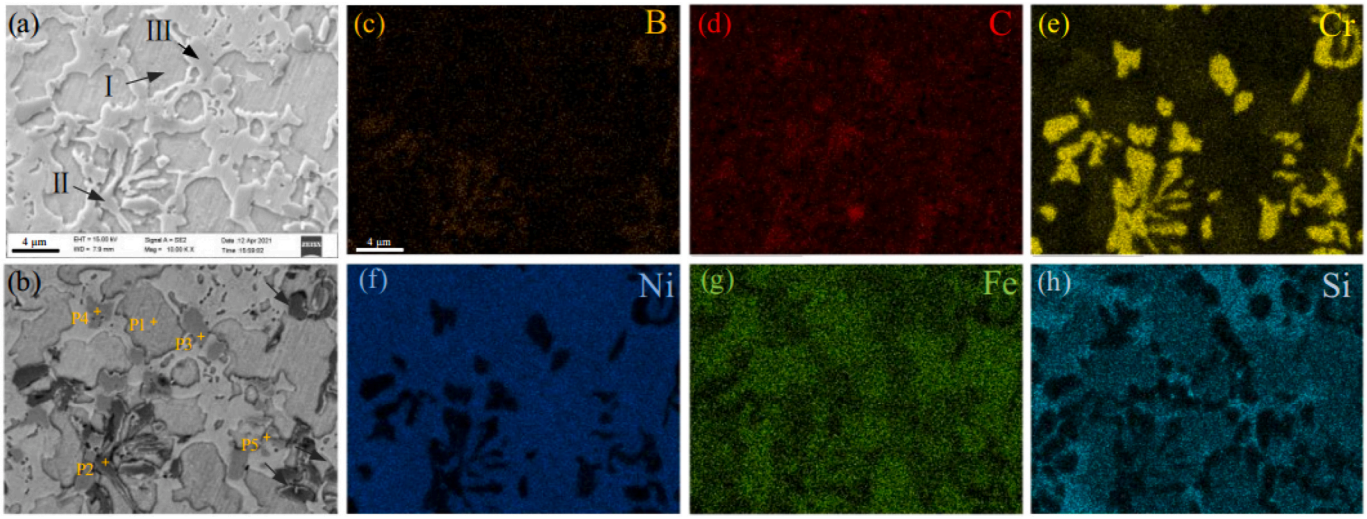


**Fig. 7.** (a) The typical SEM and (b) BSE images of Ni45 coating; (c)–(h) corresponding face distribution of element B, C, Cr, Ni, Fe, Si.

**Table 4**
Elemental composition (at. %) of various phases from EDS results.

| Element | Marked in Fig. 7 corresponding to Ni45 coating | | | | | Marked in Fig. 8 corresponding to coating 2 | | | | | Marked in Fig. 9 corresponding to coating 2# | | | | |
|---|---|---|---|---|---|---|---|---|---|---|---|---|---|---|---|
| (at. %) | P1 | P2 | P3 | P4 | P5 | P6 | P7 | P8 | P9 | P10 | P11 | P12 | P13 | P14 | P15 |
| Ti | – | – | – | – | – | 53.29 | 47.87 | 0.46 | 0.3 | – | 52.27 | 52.64 | 55.07 | 50.57 | 44.5 |
| N | – | – | – | – | – | – | | – | – | – | – | – | 44.93 | 17.06 | 28.57 |
| C | 1.07 | 17.40 | 23.78 | 18.07 | 16.77 | 46.38 | 45.76 | 21.93 | 31.43 | 11.93 | 47.39 | 47.36 | – | 31.68 | 25.94 |
| Cr | 7.48 | 31.37 | 3.63 | 5.99 | 5.21 | – | 5.56 | 50.1 | 45.5 | 24.5 | – | – | – | | – |
| B | 4.97 | 43.02 | 16.50 | 18.01 | 8.17 | – | – | 14.35 | 11.61 | 20.2 | – | – | – | | |
| Si | 6.15 | 0.47 | 7.61 | 5.16 | 6.36 | – | – | 0.48 | – | 3.72 | – | – | – | | |
| Fe | 8.24 | 2.45 | 4.57 | 6.95 | 7.33 | – | – | 5.10 | 5.17 | 5.22 | – | – | – | 0.26 | 0.57 |
| Ni | 72.09 | 5.28 | 43.91 | 45.81 | 56.16 | 0.32 | 0.81 | 7.58 | 5.98 | 34.43 | 0.34 | | – | 0.43 | 0.42 |

precipitated TiC particles is between regular quadrilateral and flower-like, which is mainly influenced by the solute concentration and growth time [29,36]. Previous studies [19,45] have indicated that the *in-situ* reaction of TiC ceramics should have sufficient mass concentration and nucleation driving force, finally resulting in the regular shape of ceramic phases [34]. However, the larger single-pass morphology is in one-to-one correspondence with the solidification time [46], which can provide enough time for the growth of the secondary precipitated TiC and eventually generate the petal-like TiC [36]. According to Fig. 8(d–f), Cr(B, C) compounds are rod-shaped with long length and dispersed small lump-shaped. The EDS results of P8 and P9 (listed in Table 4) show that the atomic ratios of Cr and C elements are close to 3:7 and 3:2, which can correspond to $Cr_3C_7$ and $Cr_3C_2$, respectively. Wu et al. [47] reported that the Gibbs free energy of $Cr_3C_7$ is lower than that of $Cr_3C_2$, thus $Cr_7C_3$ phases precipitated preferentially from the metal liquid, and then grew to a larger shape. Comparative analysis of the distribution of Ti, Cr, and C elements indicate that dispersed small-size $Cr_3C_2$ is mainly distributed around TiC particles. In particular, in region Ⅳ of Fig. 7(b), this phenomenon is more obvious. The decomposition of TiC could indeed increase the concentration of C element nearby, which is beneficial to promote the Cr element to retain these rich C regions, thus forming fine $Cr_3C_2$ during the rapid solidification process. Notably, LC has the characteristics of rapid solidification, the similarity of the thermal diffusion coefficient of each phase can often reduce the tensile stress in the solidification process, and result in fewer micro-cracks in the solidified coating [12]. Given that the thermal expansion coefficient of $Cr_3C_2$ ($10.3 \times 10^{-6}$/K) is between that of TiC ($7.74 \times 10^{-6}$/K) and metal nickel ($13.3 \times 10^{-6}$/K), the generation of $Cr_3C_2$ at the edge of TiC can weaken the crack sensitivity in the region between the ceramic phases and matrix, which is beneficial to reduce the spalling of ceramic phases during wear test [24].

The surface distribution of Ti, B, C, N, Cr, Ni, and Fe elements of coating 2# is shown in Fig. 9. Clearly, the distribution position of the Ti element exactly corresponds to that of the C and N elements. Fig. 9(e) and (f) and XRD results (Fig. 6) indicate that these Ti-rich regions can be roughly composed of TiC, TiN, and Ti (C, N) ceramic phases. EDS results of P11 to P12 show that these C-rich regions shown in Fig. 8(e) should be TiC. Comparative analysis of Fig. 9(e) and (f) reveal that a small part of TiN got dissolved into TiC particles. Fig. 9(a) shows the existence of an agglomerated large TiN particle (length > 20 μm) in region V-1. Noteworthy, the [C] atoms were found to surround the TiN particles in region V-2 as shown in Fig. 9(e). TiC and TiN show the same lattice structure, as

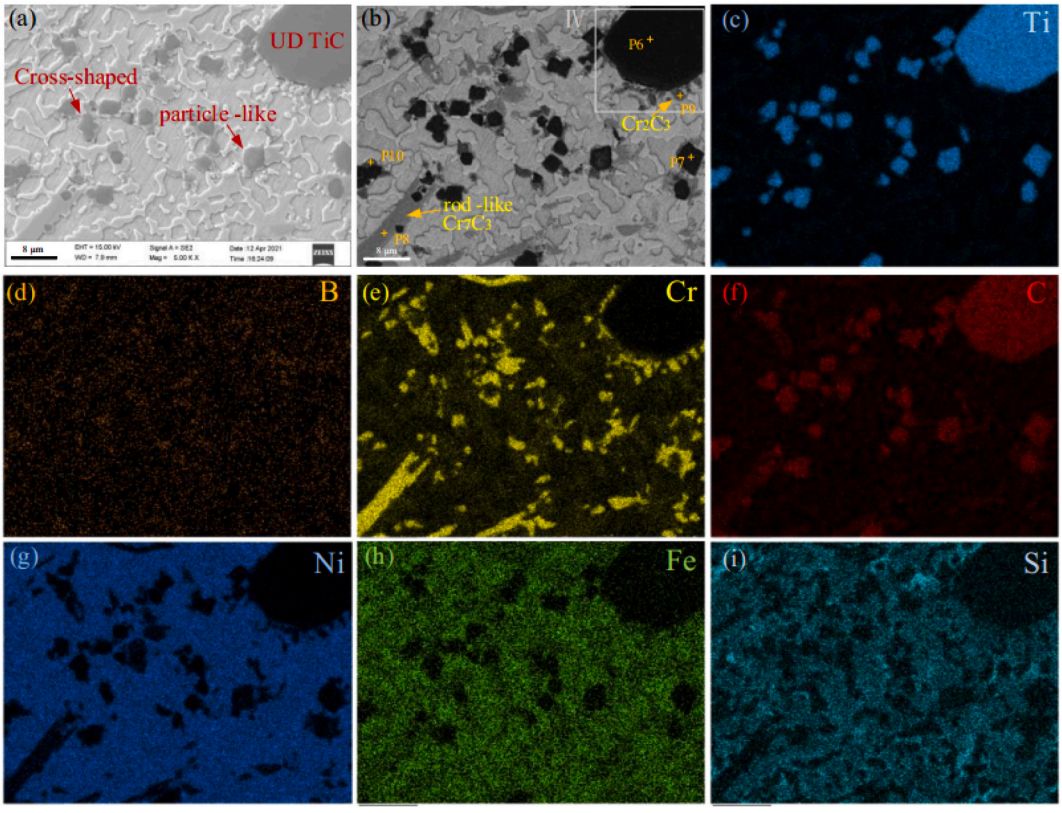


**Fig. 8.** (a) The typical SEM and (b) BSE images of coating 2; and (c)–(i) corresponding surface distribution of elements Ti, B, Cr, C, Ni, Fe, Si.

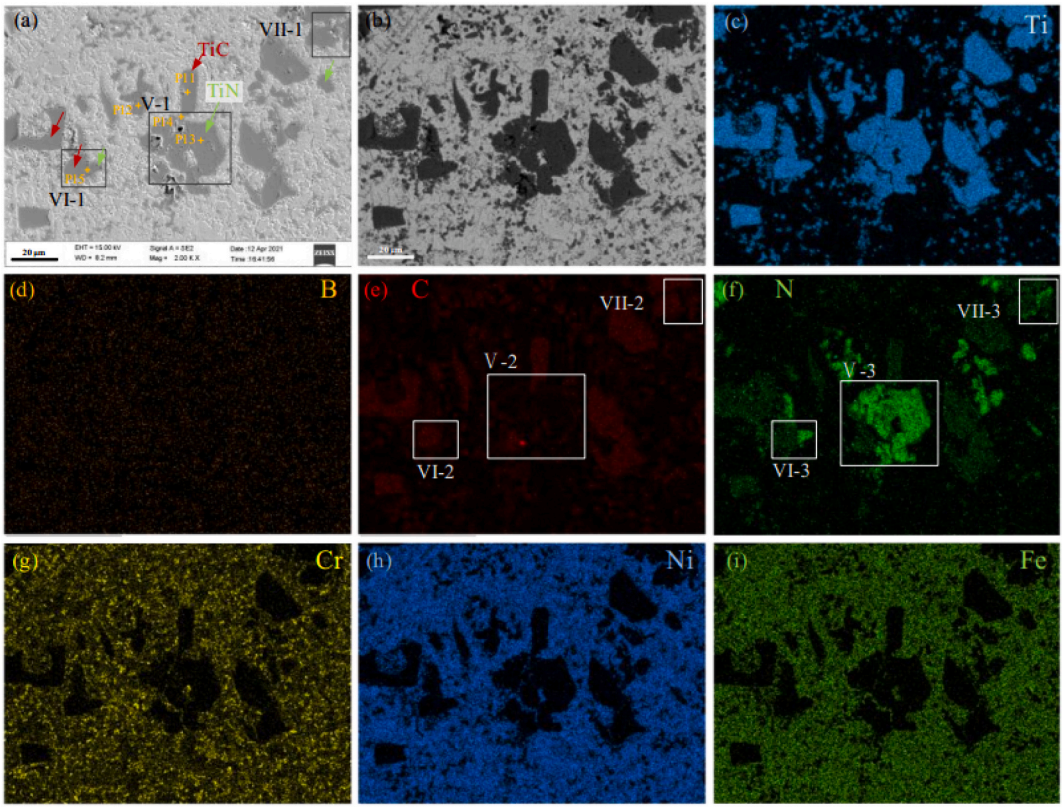


**Fig. 9.** (a) The typical SEM and (b) BSE images of coating 2#; (c)–(i) corresponding surface distribution of element Ti, B, C, N, Cr, Ni, Fe.

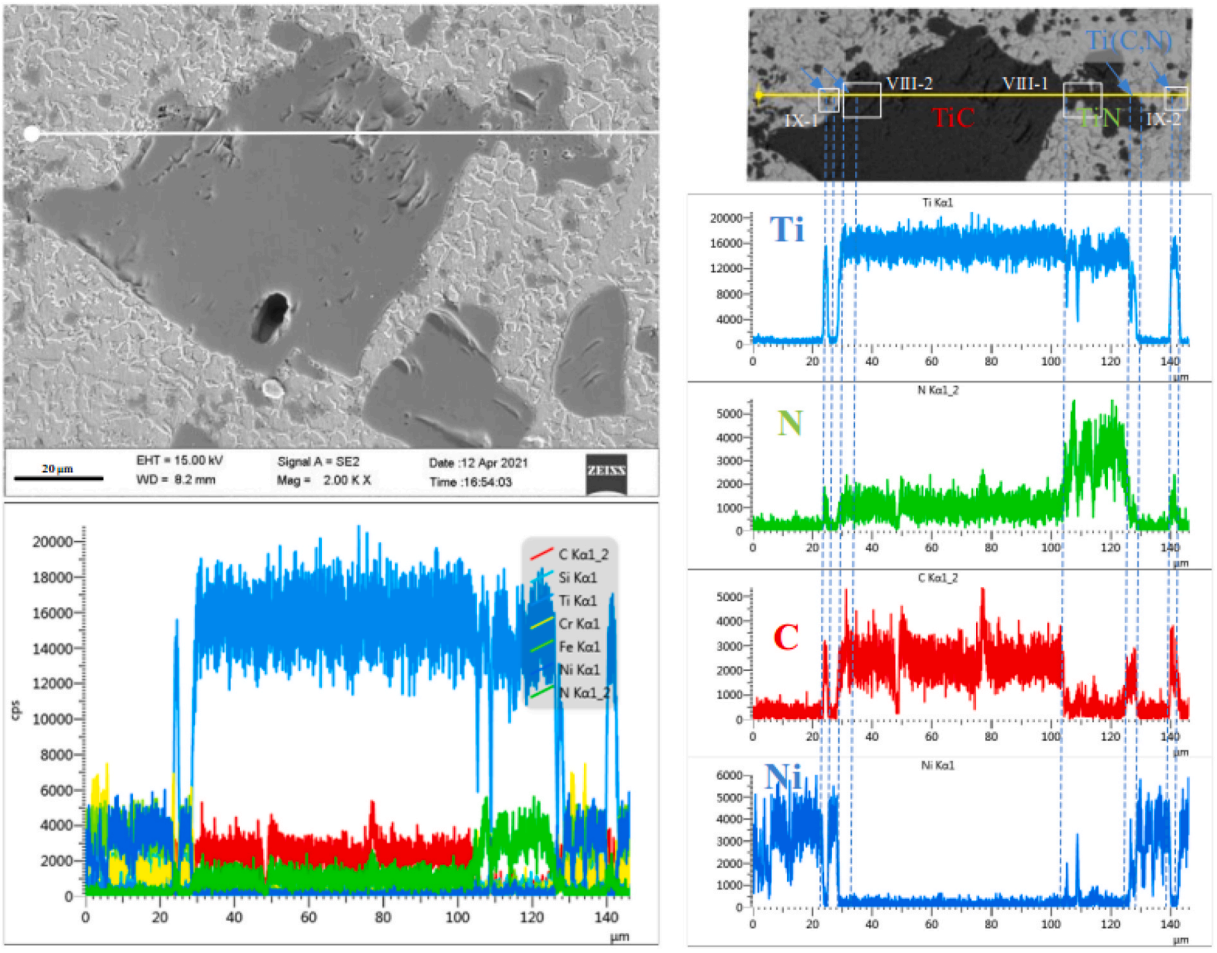


**Fig. 10.** The results of EDS line scanning from coating 2#.

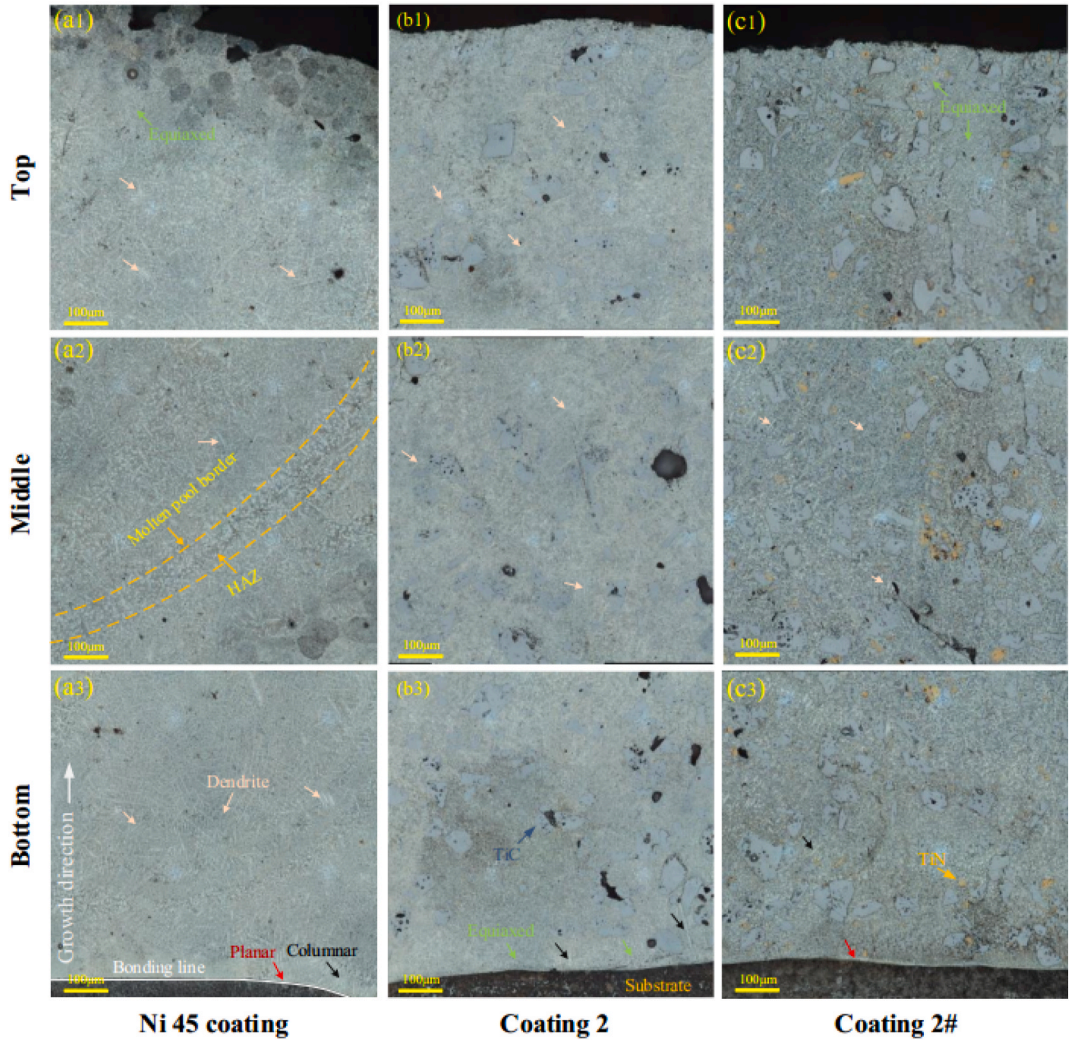


**Fig. 11.** The optical microstructure of coatings. (a1)–(c1) Microstructure on top region; (a2)–(c2) microstructure on middle region; and (a3)–(c3) microstructure on bottom region.

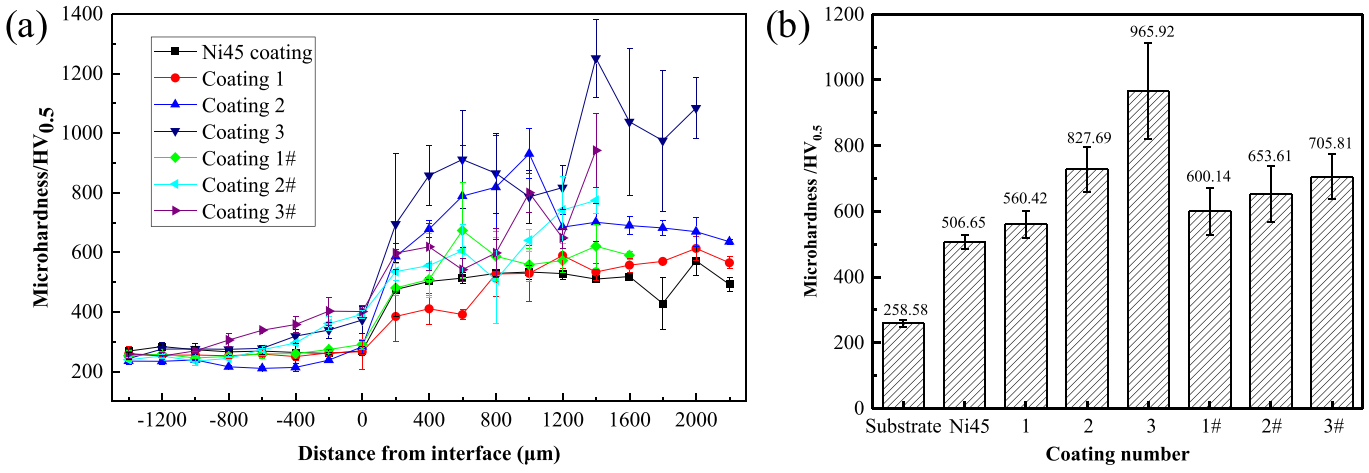


**Fig. 12.** Cross-section hardness of different coatings: (a) the hardness curves; (b) average hardness.

a result, their [C] and [N] atoms can be completely exchanged. Therefore, the ring-shaped Ti (C, N) was *in-situ* synthesized around the TiN particle according to the EDS result of P14. The region VI-1 shown in Fig. 9(a) indicates that the diffusion between [C] and [N] atoms during the solidification process resulted in the formation of the Ti (C, N) phase in the bonding region between TiC and TiN. In contrast with regions VII 1–3, Ti (C, N) phases are also found around the TiC particles. To further analyze the distribution of elements around TiC and TiN particles, EDS

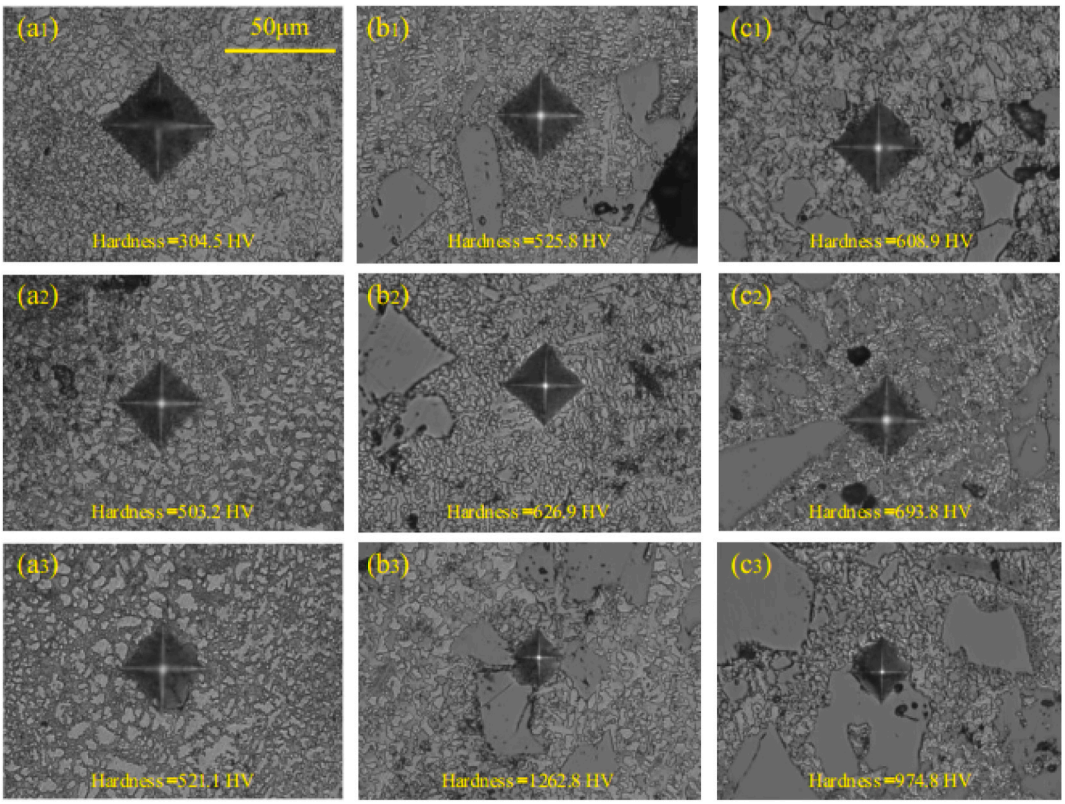


**Fig. 13.** The 40x images of hardness indentation for (a1)–(a3) Ni45 coating, (b1)–(b3) coating 2, and (c1)–(c3) coating 2#.

line scanning of Ti, C, N, and Ni elements from the coating 2# was carried out, and the results are presented in Fig. 10. The content of the N element at the edge of TiC particles increases obviously, which indicates that a part of TiN dissolves into TiC, and results in the formation of ring-shaped Ti(C, N) phases. The Ni element on the right side of the TiC phase (region VIII-1) is much smoother than that on the left side of the TiC phase (region VIII-2). This illustrates that coarse TiC particle is well bonded with the γ-Ni (Fe) matrix. The regions IX-1 and IX-2 shown in Fig. 10 indicate that the secondary precipitated black granular phases with small size are mainly composed of Ti, C, and N elements, which can be considered as Ti(C, N) phases according to XRD results. EDS analysis results show that a new interface structure (Ti(C, N) phases) is formed in the bonding region between the coarse TiC phases and the matrix due to the addition of fine TiN. These *in situ* generated Ti (C, N) phases not only combine the individual advantages of TiC with high hardness and TiN with sufficient toughness, but also show excellent conductivity and chemical stability [48]. Moreover, the new interface structure is conducive to reduce residual thermal stress and restrain crack growth [49]. Therefore, these *in-situ* generated Ti (C, N) phases around the large-size TiC particles are beneficial to promote the metallurgical bonding between the ceramic phases and the matrix.

### 3.3. Microstructural characterization

The three regions of the optical microstructure of Ni45 coating, coating 2, and coating 2# are shown in Fig. 11. Fig. 11(a1)–(a3) exhibit that the Ni45 coating is mainly composed of planar crystal, columnar crystal, dendrite crystal, and equiaxed crystal from bottom to top. This is a typical microstructure characteristic of the rapidly solidified alloy coating prepared by AM technology [50,51]. When 20 wt% TiC particles were added to the Ni45 powders, the microstructure of the solidified coating 2 was refined compared to that of the Ni45 coating. In the bonding region between coating and substrate, the number and size of columnar grains perpendicular to the bonding line are reduced. It is well known that the large temperature gradient ($G$) and the low solidification rate ($R$) promote the formation of columnar crystals [52]. During the rapid solidification process of coating 2, the TiC with low thermal conductivity could reduce the directivity of $G$ by its pinning effect. This phenomenon not only prevents the growth of columnar crystals but also promotes the desired columnar to equiaxed transition (CET), which is beneficial to the improvement of the mechanical properties of metal parts manufactured by AM [53]. Due to the layer-by-layer manufacturing property of AM technology, the microstructure at the molten pool border is often different from that in the deposited layer. This phenomenon often leads to sudden changes in hardness, wear resistance, tensile strength, and other mechanical properties, thus reducing the service life of parts [54,55]. Noteworthy, no obvious molten pool border is found in coating 2 (Fig. 11b2). This can significantly reduce the fluctuation of the mechanical properties of the MMC coatings. In particular, the growth direction of dendrite crystals at the top of coating 2 is perpendicular to that of coating (Fig. 11b1), which is opposite to that of columnar crystal at the bottom. This is mainly attributed to the fact the heat loss was hindered by the TiC particles at the top of coating 2, and the heat transfer gradually changed from vertical to horizontal. The finding of planar crystal indicates that coating 2# exhibits good metallurgical bonding with the substrate [56]. At the same time, the undesired columnar crystals were not found at the bottom of the coating 2# due to the addition of TiC and TiN. The addition of TiN could refine the size of TiC (Fig. 5), and promote the secondary precipitation of fine TiC particles. This precipitated fine TiC could effectively reduce the $G$ during the solidification process, and promote CET. Analysis of microstructural evolution indicated that the addition of ceramic particles could weaken the direction of the thermal gradient during the solidification process. Thus, there was no obvious grain without any specific orientation in ceramic reinforced composite coatings. This phenomenon is beneficial to improve the uniformity of mechanical properties of the coatings.

### 3.4. Mechanical properties

#### 3.4.1. Hardness

Fig. 12 exhibits the hardness distributions of each coating along the growth direction and their average values as well. The average hardness of Ni45 coating is 506.65 ± 22.58 $HV_{0.5}$, which is consistent with that reported by Sun et al. [43], and 1.7 times that of Ni25 coating with the 298 $HV_{0.2}$ obtained in the previous study [51]. The high hardness of Ni45 coating is mainly attributed to the dispersive distribution of *in-situ* formed hard phases Cr(C, B) (Figs. 6 and 7). Fig. 13(a1)–(a3) depict microstructure around hardness indentations of Ni45 coating. XRD and EDS results together indicate that the bright block microstructure is γ-Ni (Fe) solid solution with low hardness, and the local black microstructure is mainly composed of Cr(C, B) phases with high hardness. Fig. 13(a1) and (c1) exhibit significant differences in hardness. The main reason for this phenomenon is the existence of HAZ in the lapping region [54]. When 10 wt% coarse TiC particles were added to the coating, the hardness of the coating was narrowly improved. The low hardness for coating 1 (560.42 ± 41.56 $HV_{0.5}$) is mainly attributed to the oxidation of a large amount of TiC, resulting in the highest porosity (20.415%) and the smallest volume fraction (7.028 %) of ceramic phases. When the volume fraction of the ceramic phases increases from 27.110 to 48.403 %, the hardness of coatings 2 and 3 are 727.69 ± 67.13 and 965.92 ± 147.07 $HV_{0.5}$, which are 2.81 and 3.74 times higher than that of the substrate (258.58 $HV_{0.5}$), and 1.44 and 1.91 times higher than that of Ni45 coating, respectively. Noteworthy, hardness distribution in coatings 1–3 is non-uniform. Fig. 13(b1)–(b3) exhibit that some indentations are distributed on or around the UD TiC particles in coating 2, resulting in a sudden increase in hardness. Figs. 5 and 12(b) demonstrate that, with the addition of 2 wt% TiN, the hardness of coating 1# is 39.72 HV higher than that of coating 1, which is not obviously in correspondence with the increase of ceramic phase volume fraction. Besides, the volume fraction of ceramic phases in coatings 2 # and 3 # is significantly larger than that of coating 2 and 3, respectively, while their microhardness is 74.08 HV and 260.11 HV lower than those of the corresponding coatings. The previous study [48] demonstrated that TiN particles could effectively improve the toughness of metal matrix composites. In general, the toughness and hardness of materials tend to have the opposite trend. Moreover, the hardness of added TiN particles (about 2400 HV) is lower than that of TiC (about 3000 HV). Therefore, although the addition of TiN improves the volume fraction of the ceramic phase, the increase in the hardness of the composite coating is not obvious. The addition of TiN is conducive to the precipitation of fine TiN and Ti(C, N) phases (Fig. 13c1–c3), and can further reduce the fluctuation of coating hardness, as shown in Fig. 12. Furthermore, the hardness of each coating increases gradually from the substrate to the top of the coating, and no obvious step is observed in hardness at the interface between coating and substrate. The transformation from α-Ni(Fe) to martensite is expected to take place in the HAZ of the matrix during rapid heating and cooling, which is beneficial for promoting the smooth transition of stress and strain between the composite coating with high hardness and the substrate with low hardness.

#### 3.4.2. Wear resistance

The wear resistance of MMC coatings is an important index to evaluate their service life, which can be evaluated by using friction coefficient, wear rate, and worn surface. Fig. 14 displays the plots of the COFs versus wear time and wear rate for different composite coatings. Fig. 14(a) exhibits that the COFs of all coatings show a running-in step at the beginning of the test, and then the wear process tends to a steady wear regime after about 20 min. Moreover, it was found that the COFs of the composite coating containing the ceramic phase are more stable than those of Ni45 coating and substrate during the steady wear regime. In particular, the fluctuations of COFs of coatings 2# and 3# with the addition of fine TiN are reduced further. The reinforced phases (TiC, TiN, Ti(C, N) and Cr(B, C)) with high hardness play the role of a "skeleton" and transfer more contact stress to themselves during the wear test, which could prevent the micro-cutting of the γ-Ni(Fe) matrix and effectively reduce the contact area, thus improving the wear resistance of the coating. The average COF of each coating was sampled in the last 40 min. The wear rate (ω) of the coatings ($mm^3 \cdot N^{-1}\ m^{-1}$) could be obtained by using $\omega = V_{loss}/(W \cdot L)$ [57], where $V_{loss}$ is the volume loss (measured using laser confocal microscopy), W is constant load (15 N) and L is the wear distance (wear time × wear speed). The average COFs and wear rate of each coating are shown in Fig. 14(b). Obviously, the average COFs of the substrate, Ni45 coating, and MMC coatings with different coarse TiC and fine TiN contents are 0.613, 0.579, 0.538, 0.465, 0.513, and 0.409, respectively, and the corresponding wear rates are 138.16, 90.23, 86.41, 63.33, 63.41 and 42.44 × $10^{-6}$ $mm^3\ N^{-1}\ m^{-1}$, respectively. Coating 3# exhibits the best wear resistance, and its average COF and wear rate are 0.667 and 0.307 times those of the substrate, respectively. Furthermore, the COFs and wear rate of each coating show almost the same trend. Interestingly, although the micro-hardness of coatings 2#–3# is lower than that of coatings 2 and 3, they exhibit better wear resistance. This is against Archard's law that the wear resistance of a material is proportional to its hardness [58]. As mentioned above, the generation of *in-situ* ring-shaped Ti (C, N) phases around the coarse TiC and TiN particles would enhance the bonding force between the ceramic phases and the matrix, thus reducing the wear rate.

The 3D surface topographies, profile curves, and worn surfaces of coatings were measured by laser confocal microscopy to reveal the wear

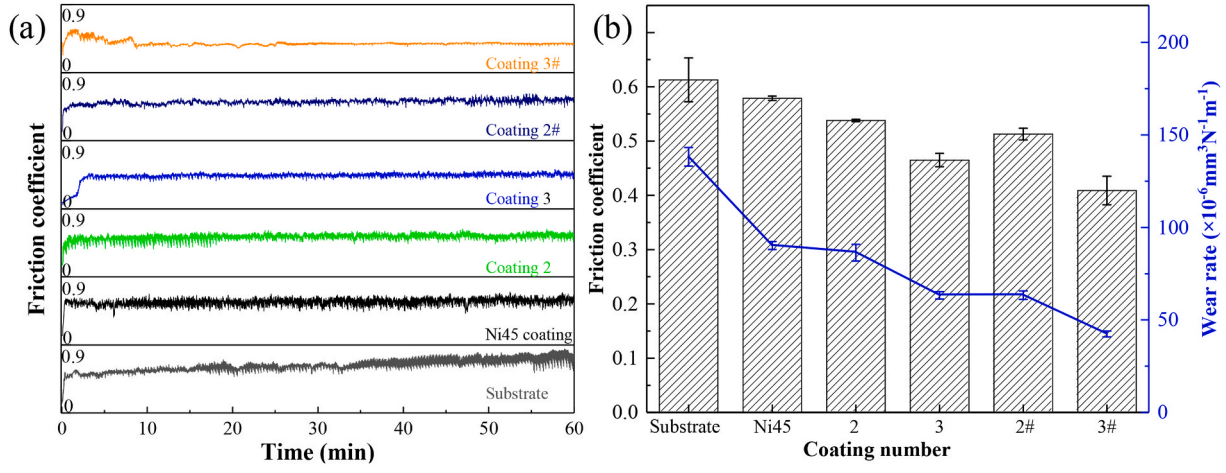


**Fig. 14.** (a) COF curves versus time and (b) average COF and wear rate of each coating.

mechanisms in detail. Fig. 15(a1–a3) demonstrate that the wear track of the substrate is wide and deep with a maximal area of 5891.846 μm$^2$. Moreover, slight plastic deformation and small grooves are present on the worn surface, owing to the low microhardness (258.58 $HV_{0.5}$). During the wear process, the hard asperities of $ZrO_2$ could easily infiltrate into the worn surface of the 40Cr substrate, leading to plastic deformation and micro-cutting and resulting in smaller grooves. Thus, the wear characteristics of the substrate can be inferred as the

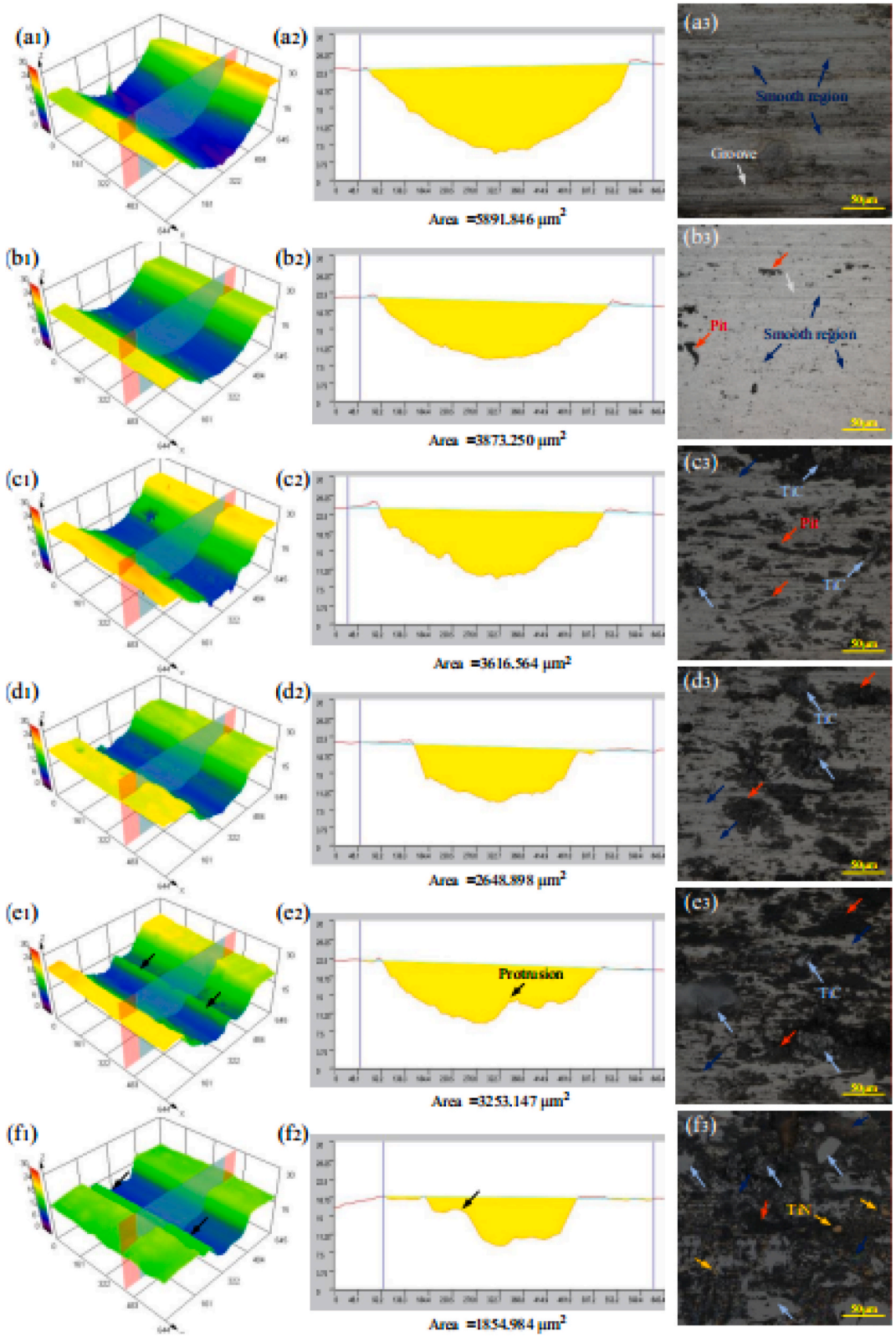


**Fig. 15.** The 3D surface topographies, profile curves and worn surfaces of (a1–a3) substrate; (b1–b3) Ni45 coating; (c1–c3) coating 2; (d1–d2) coating 3; (e1–e2) coating 2#; (f1–f3) coating 3#.

combination of abrasive and adhesive wear. In comparison, due to the dispersion strengthening of hard phases (Cr-(B, C)) and the solid solution strengthening of intermetallic compounds TiNi, the cross-sectional area of Ni45 coating is significantly reduced, and no obvious grooves are found on the worn surface. Besides, some small pits appear on the worn surface of the Ni45 coating. The deformation of these hard phases under the action of the reciprocating stress is lower than that of the matrix during the testing process, which leads to micro-cracks at the edge of the hard phases, and the formation of pits in serious cases [59]. When the volume fraction of coarse TiC increases from 27.11 % to 48.40 %, shallow pits and small grooves appear on the worn surface of coatings 2 and 3 (Fig. 15c3 and d3), although the wear rate is reduced. The locations of TiC and pits on the worn surface are consistent. The toughness of the material is often inversely proportional to its hardness [60]; therefore, it is difficult for friction pair ($ZrO_2$) to squeeze the coarse TiC into the Ni45 matrix during the wear test. This can result in the fracture on the surface of the coarse TiC with high hardness and limited toughness, which gradually turns into small flakes. With the progress of reciprocating friction, these lamellar TiC phases (located in the coarse TiC) then fall off from the matrix, and pits are formed. This phenomenon may worsen the surface quality of the wear track, which is disadvantageous to improve the service life of the material. Compared to coatings 2 and 3, the protrusion on coatings 2 # and 3 # worn surface along the wear direction indicates that their deformation resistance becomes stronger, thus further reducing the size of the wear track. This phenomenon can be attributed to enough toughness of the coatings, which can also be demonstrated by the less spalling of ceramic phases on the worn surface (Fig. 15e3 and f3). There are two reasons for the improvement of the toughness of the coating with the fine addition of TiC. On the one hand, the addition of fine TiN refined the large particle ceramic phases (Fig. 5). On the other hand, the *in-situ* formed (C, N) phases are distributed on the edge of coarse TiC particles and further reduce the crack sensitivity. According to the above-mentioned analysis, the worn surfaces of coatings 2# and 3# show a typical spalling phenomenon, thus the wear mechanism is adhesive wear and abrasive wear.

### 3.5. Repair process

To verify the feasibility of the MMC coatings with respect to surface repair, given the advantages of the formability, microstructure, and mechanical properties, coatings 2 and 2# were selected as the repair materials for the surface defects of the spline shaft. Fig. 16 presents the additive/subtractive hybrid repairing process for damaged parts. It was found that the main failure form of the waste spline shaft was plastic deformation as shown in Fig. 16(a). According to the literature [14,15,61], the shape of the designed groove to be filled and scanning strategy are the two crucial factors for deciding the formability, microstructure distribution, residual stress, and mechanical properties of the repaired zone. Fig. 16(b) exhibits the dimensions of the parts to be repaired by reverse engineering and the designed grooves to be filled. The depth of the groove is selected to be 1.0 mm, which is the median value recommended by Hutasoit et al. [62]. The process of LC to fill the designed grooves and the experimental results are shown in Fig. 16(c). The topography of the repaired zones are relatively flat, which is beneficial to the subsequent machining. For exploring the machining performance of the composite coating, a wire electrical discharge machining was used to remove the redundant materials on the coating surface, and the machining allowance for the subsequent grinding was 100 μm. The grinding parameters for the composite coatings 2 and 2# are cutting depth ~50 μm, feed rate ~1 m/min, grinding speed ~10 m/s, and resin bonded CBN grinding wheel with φ80 mm and abrasive size of 80 #. The macro morphology of the repaired zone after grinding is shown in Fig. 16(d).

After grinding, the machined 2D and 3D surface morphologies and corresponding roughness on the substrate and repaired zones by coating 2 and 2# are shown in Fig. 17. Ten lines perpendicular to the grinding direction were randomly selected, and their average roughness was taken as the roughness (Ra) of the entire machined surfaces. Fig. 17(a) exhibits that the machined substrate surface presents a typical grinding morphology. The grinding groove is long and deep, and the surface roughness is the largest with 0.46 μm among all machined surfaces. When 20 wt% TiC is added to the Ni45 powder, the number and length of grooves in the repaired region by coating 2 are significantly reduced. However, some deeper and wider grooves are also found, as shown in Fig. 17(b). This phenomenon may be attributed to abrasive wear during the grinding process caused by easily exfoliated TiC particles. At the same time, some pits caused by TiC spalling are also observed, which can provide a theoretical basis for the formation of these large grooves. According to the previous analysis, the holding force of the matrix of coating 2# to the ceramic phase is significantly higher than that of coating 2. Therefore, the surface quality of the ground coating 2# is the best with the smallest surface roughness and the minimum number of grooves (Fig. 17(c)). Furthermore, some cracks are also found on the machined surface of the composite coatings, which are mainly caused by the large thermophysical parameters between the ceramic phase and the substrate, which is not conducive to improving the accuracy of the parts after machining. Previous studies [63,64] have shown that additional assisted field is an effective method to improve the machining accuracy of composite materials. Noteworthy, the roughness of the composite coating 2# after grinding is 0.39 μm, which is lower than that of the substrate and is almost consistent with that of the steel after traditional grinding [65,66]. This shows that the machinability of ceramic reinforced composites is good, and it can be effectively extended to actual industrial production.

## 4. Conclusions

In this study, laser-cladding coarse TiC reinforced Ni-based

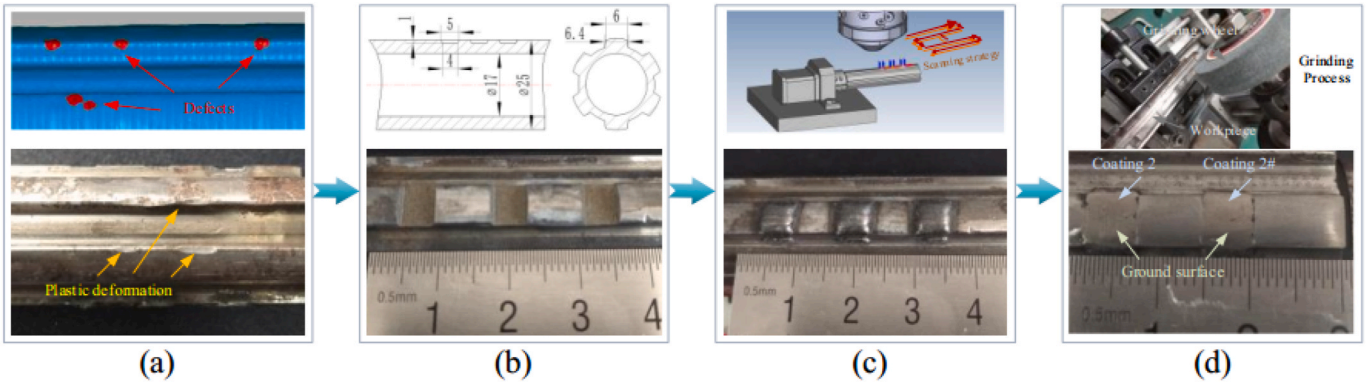


**Fig. 16.** The additive/subtractive hybrid repairing process for damaged parts.

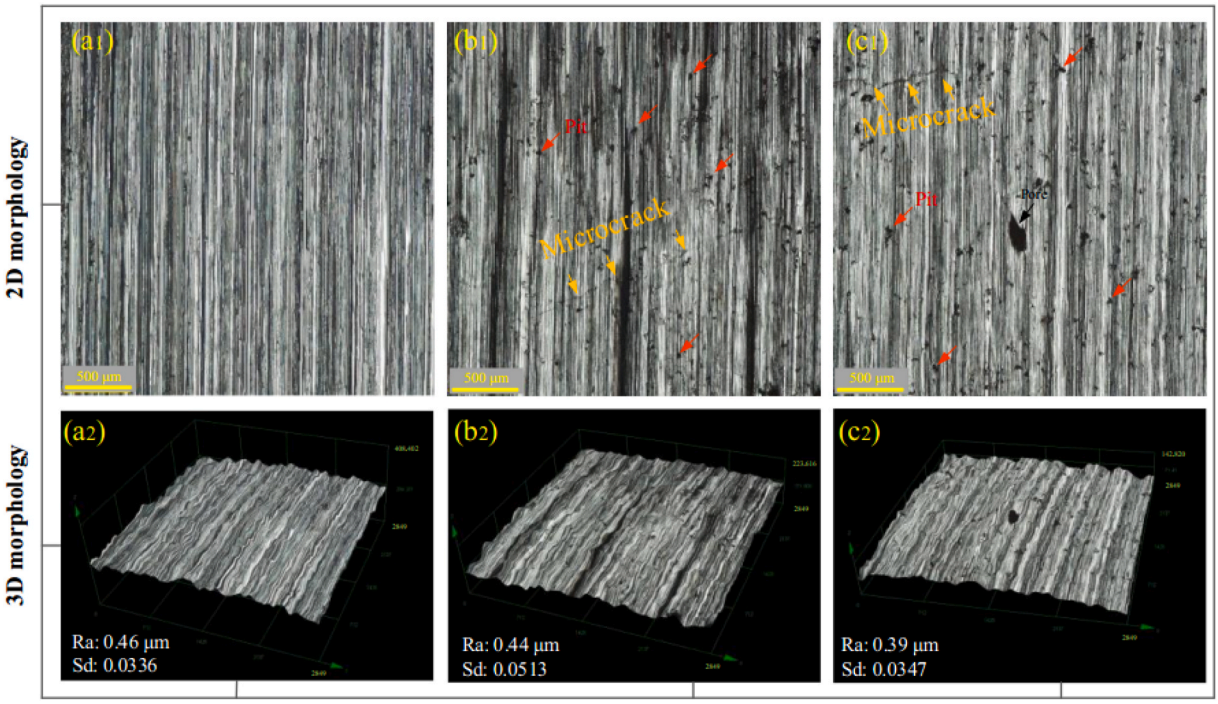


**Fig. 17.** The machined 3D surface morphologies of the repaired zones.

composite coatings were applied for repairing the surface of the damaged 40Cr spline shaft. The effects of the addition of coarse TiC and fine TiN with different contents on the formability, phase composition, microstructure, and mechanical properties were studied first in detail. Then, the waste spline shaft was repaired to verify the feasibility of MMC coatings in repairing damaged parts, and the finishing surface by grinding process was obtained, finally. The main conclusions are drawn from this study as follows:

1. The decrease of gas pores in the MMC coatings is attributed to the reduction of solidification time and the formation of desired Ti (C, N) phases by the penetration of [C] atoms into TiN particles. The volume fraction of the hard phases can be obtained from 7.03% to 48.40% by adjusting the composition of alloy elements in the precursors.
2. The phase composition and morphologies of the composite coating were determined by using the composition of elements in precursors. The main ceramics in original Ni45–TiC coatings are coarse TiC (length: 45–55 μm), CrB, Cr3C7, and Cr3C2. With fine the addition of TiN, *in-situ* synthesized ring-shaped Ti (C, N) phases are present at the edges of both undissolved TiC and TiN particles, which improves the metallurgical bonding between ceramics and γ-Ni(Fe) matrix.
3. The coarse ceramic particles with low thermal conductivity are distributed homogeneously in the composite coating, which is beneficial to promote the desired columnar to equiaxed transition and eliminate the heat-affected zone.
4. The average hardness of the MMC coatings increases from 560.42 $HV_{0.5}$ to 965.92 $HV_{0.5}$. The average hardness of the MMC coating decreases due to the addition of fine TiN, while the toughness is increased. The Ni45-30 wt% TiC-6 wt.% TiN coating exhibits the best wear resistance, and its wear rate is 42.44 × $10^{-6}$ $mm^3$ $N^{-1}$ $m^{-1}$, which is 0.307 times that of the 40Cr substrate.
5. The ceramic reinforced MMC coatings can realize the surface repair of waste parts combined with additive/subtractive hybrid manufacturing technology.

## Declaration of competing interest

The authors declare that they have no known competing financial interests or personal relationships that could have appeared to influence the work reported in this paper.

## Acknowledgments

This work was financially supported by the Fundamental Research Funds for the Central Universities (N2103004), and the National Natural Science Foundation of China (52075088).

## References

[1] Z. wei Yu, X. lei Xu, Z. Yang, Y. yuan Li, Case internal oxidation and intergranular fracture of carburized splined-shaft, Eng. Fail. Anal. 22 (2012) 141–151, https://doi.org/10.1016/j.engfailanal.2012.01.016.
[2] L.J. Shen, A. Lohrengel, G. Schäfer, Plain-fretting fatigue competition and prediction in spline shaft-hub connection, Int. J. Fatig. 52 (2013) 68–81, https://doi.org/10.1016/j.ijfatigue.2012.11.012.
[3] Z. Liu, Q. Jiang, T. Li, S. Dong, S. Yan, H. Zhang, B. Xu, Environmental benefits of remanufacturing: a case study of cylinder heads remanufactured through laser cladding, J. Clean. Prod. 133 (2016) 1027–1033, https://doi.org/10.1016/j.jclepro.2016.06.049.
[4] H. Zheng, E. Li, Y. Wang, P. Shi, B. Xu, S. Yang, Environmental life cycle assessment of remanufactured engines with advanced restoring technologies, Robot. Comput. Integrated Manuf. 59 (2019) 213–221, https://doi.org/10.1016/j.rcim.2019.04.005.
[5] X. Zhang, M. Zhang, H. Zhang, Z. Jiang, C. Liu, W. Cai, A review on energy, environment and economic assessment in remanufacturing based on life cycle assessment method, J. Clean. Prod. 255 (2020), 120160, https://doi.org/10.1016/j.jclepro.2020.120160.
[6] J. Shi, S.Q. Bai, Research on gear repairing technology by laser cladding, Key Eng. Mater. 546 (2013) 40–44. https://doi.org/10.4028/www.scientific.net/KEM.546.40.
[7] Y. Li, Q. Han, I. Horváth, G. Zhang, Repairing surface defects of metal parts by groove machining and wire + arc based filling, J. Mater. Process. Technol. 274 (2019), 116268, https://doi.org/10.1016/j.jmatprotec.2019.116268.
[8] A. Saboori, A. Aversa, G. Marchese, S. Biamino, M. Lombardi, P. Fino, Application of directed energy deposition-based additive manufacturing in repair, Appl. Sci. 9 (2019), https://doi.org/10.3390/app9163316.
[9] A.A. Siddiqui, A.K. Dubey, Recent trends in laser cladding and surface alloying, Opt Laser. Technol. 134 (2021), 106619, https://doi.org/10.1016/j.optlastec.2020.106619.

[10] H. Tan, W. Shang, F. Zhang, A.T. Clare, X. Lin, J. Chen, W. Huang, Process mechanisms based on powder flow spatial distribution in direct metal deposition, J. Mater. Process. Technol. 254 (2018) 361–372, https://doi.org/10.1016/j.jmatprotec.2017.11.026.
[11] A. Ray, K.S. Arora, S. Lester, M. Shome, Laser cladding of continuous caster lateral rolls: microstructure, wear and corrosion characterisation and on-field performance evaluation, J. Mater. Process. Technol. 214 (2014) 1566–1575, https://doi.org/10.1016/j.jmatprotec.2014.02.027.
[12] T. DebRoy, H.L. Wei, J.S. Zuback, T. Mukherjee, J.W. Elmer, J.O. Milewski, A. M. Beese, A. Wilson-Heid, A. De, W. Zhang, Additive manufacturing of metallic components – process, structure and properties, Prog. Mater. Sci. 92 (2018) 112–224, https://doi.org/10.1016/j.pmatsci.2017.10.001.
[13] L. Zhu, P. Xue, Q. Lan, G. Meng, Y. Ren, Z. Yang, P. Xu, Z. Liu, Recent research and development status of laser cladding: a review, Opt Laser. Technol. 138 (2021), 106915, https://doi.org/10.1016/j.optlastec.2021.106915.
[14] Y. Li, S. Dong, S. Yan, X. Liu, P. He, B. Xu, Surface remanufacturing of ductile cast iron by laser cladding Ni-Cu alloy coatings, Surf. Coating. Technol. 347 (2018) 20–28, https://doi.org/10.1016/j.surfcoat.2018.04.065.
[15] W.J. Oh, W.J. Lee, M.S. Kim, J.B. Jeon, D.S. Shim, Repairing additive-manufactured 316L stainless steel using direct energy deposition, Opt Laser. Technol. 117 (2019) 6–17, https://doi.org/10.1016/j.optlastec.2019.04.012.
[16] H. Paydas, A. Mertens, R. Carrus, J. Lecomte-Beckers, J. Tchoufang Tchuindjang, Laser cladding as repair technology for Ti-6Al-4V alloy: influence of building strategy on microstructure and hardness, Mater. Des. 85 (2015) 497–510, https://doi.org/10.1016/j.matdes.2015.07.035.
[17] H. Koehler, K. Partes, T. Seefeld, F. Vollertsen, Laser reconditioning of crankshafts: from lab to application, Phys. Procedia. 5 (2010) 387–397, https://doi.org/10.1016/j.phpro.2010.08.160.
[18] L. Zhu, S. Wang, H. Pan, C. Yuan, X. Chen, Research on remanufacturing strategy for 45 steel gear using H13 steel powder based on laser cladding technology, J. Manuf. Process. 49 (2020) 344–354, https://doi.org/10.1016/j.jmapro.2019.12.009.
[19] Y. Liu, L. Yang, X. Yang, T. Zhang, R. Sun, Optimization of microstructure and properties of composite coatings by laser cladding on titanium alloy, Ceram. Int. 47 (2021) 2230–2243, https://doi.org/10.1016/j.ceramint.2020.09.063.
[20] T.G. Zhang, H.F. Zhuang, Q. Zhang, B. Yao, F. Yang, Influence of Y2O3 on the microstructure and tribological properties of Ti-based wear-resistant laser-clad layers on TC4 alloy, Ceram. Int. 46 (2020) 13711–13723, https://doi.org/10.1016/j.ceramint.2020.02.159.
[21] Y. bin Cao, S. xin Zhi, H. bo Qi, Y. Zhang, C. Qin, S. pu Yang, Evolution behavior of ex-situ NbC and properties of Fe-based laser clad coating, Opt Laser. Technol. 124 (2020), 105999, https://doi.org/10.1016/j.optlastec.2019.105999.
[22] D. Tijo, M. Masanta, In-situ TiC-TiB2 coating on Ti-6Al-4V alloy by tungsten inert gas (TIG) cladding method: Part-II. Mechanical performance, Surf. Coating. Technol. 344 (2018) 579–589, https://doi.org/10.1016/j.surfcoat.2018.03.083.
[23] H. Zhu, M. Ouyang, J. Hu, J. Zhang, C. Qiu, Design and development of TiC-reinforced 410 martensitic stainless steel coatings fabricated by laser cladding, Ceram. Int. 47 (2021) 12505–12513, https://doi.org/10.1016/j.ceramint.2021.01.108.
[24] Y. Zhao, T. Yu, L. Chen, Y. Chen, C. Guan, J. Sun, Microstructure and wear resistance behavior of Ti–C–$B_4C$-reinforced composite coating, Ceram. Int. 46 (2020) 25136–25148, https://doi.org/10.1016/j.ceramint.2020.06.300.
[25] B. AlMangour, D. Grzesiak, J.M. Yang, In-situ formation of novel TiC-particle-reinforced 316L stainless steel bulk-form composites by selective laser melting, J. Alloys Compd. 706 (2017) 409–418, https://doi.org/10.1016/j.jallcom.2017.01.149.
[26] G. Muvvala, D. Patra Karmakar, A.K. Nath, In-process detection of microstructural changes in laser cladding of in-situ Inconel 718/TiC metal matrix composite coating, J. Alloys Compd. 740 (2018) 545–558, https://doi.org/10.1016/j.jallcom.2017.12.364.
[27] Z. Zhang, X. Wang, Q. Zhang, Y. Liang, L. Ren, X. Li, Fabrication of Fe-based composite coatings reinforced by TiC particles and its microstructure and wear resistance of 40Cr gear steel by low energy pulsed laser cladding, Opt Laser. Technol. 119 (2019), 105622, https://doi.org/10.1016/j.optlastec.2019.105622.
[28] L. Chen, T. Yu, P. Xu, B. Zhang, In-situ NbC reinforced Fe-based coating by laser cladding: simulation and experiment, Surf. Coating. Technol. 412 (2021), 127027, https://doi.org/10.1016/j.surfcoat.2021.127027.
[29] H. Zeinali Moghaddam, M. Sharifitabar, G. Roudini, Microstructure and wear properties of Fe–TiC composite coatings produced by submerged arc cladding process using ferroalloy powder mixtures, Surf. Coating. Technol. 361 (2019) 91–101, https://doi.org/10.1016/j.surfcoat.2019.01.053.
[30] Y. Zhao, T. Zhang, L. Chen, T. Yu, J. Sun, C. Guan, Microstructure and mechanical properties of Ti–C–TiN-reinforced Ni204-based laser-cladding composite coating, Ceram. Int. 47 (2021) 5918–5928, https://doi.org/10.1016/j.ceramint.2020.11.054.
[31] Y. Lin, C. Jiang, Z. Lin, Q. Chen, Y. Lei, H. Fu, Laser in-situ synthesis of high aspect ratio TiB fiber bundle reinforced titanium matrix composite coating, Opt Laser. Technol. 115 (2019) 364–373, https://doi.org/10.1016/j.optlastec.2019.02.047.
[32] Y. Zhao, T. Yu, J. Sun, S. Jiang, Microstructure and properties of laser cladded B4C/TiC/Ni-based composite coating, Int. J. Refract. Metals Hard Mater. 86 (2020), 105112, https://doi.org/10.1016/j.ijrmhm.2019.105112.
[33] S. Liu, Y.C. Shin, The influences of melting degree of TiC reinforcements on microstructure and mechanical properties of laser direct deposited Ti6Al4V-TiC composites, Mater. Des. 136 (2017) 185–195, https://doi.org/10.1016/j.matdes.2017.09.063.
[34] S. Saroj, C.K. Sahoo, M. Masanta, Microstructure and mechanical performance of TiC-Inconel825 composite coating deposited on AISI 304 steel by TIG cladding process, J. Mater. Process. Technol. 249 (2017) 490–501, https://doi.org/10.1016/j.jmatprotec.2017.06.042.
[35] J. Wang, L. Li, P. Lin, J. Wang, Effect of TiC particle size on the microstructure and tensile properties of TiCp/Ti6Al4V composites fabricated by laser melting deposition, Opt Laser. Technol. 105 (2018) 195–206, https://doi.org/10.1016/j.optlastec.2018.03.009.
[36] H. Chen, Y. Lu, Y. Sun, Y. Wei, X. Wang, D. Liu, Coarse TiC particles reinforced H13 steel matrix composites produced by laser cladding, Surf. Coating. Technol. 395 (2020), 125867, https://doi.org/10.1016/j.surfcoat.2020.125867.
[37] Y. Cai, Z. Luo, Y. Chen, S. Ao, Influence of $CeO_2$ on tribological behaviour of TiC/Fe-based composite coating, Surf. Eng. 33 (2017) 936–943, https://doi.org/10.1080/02670844.2017.1309742.
[38] L. Yang, T. Yu, M. Li, Y. Zhao, J. Sun, Microstructure and wear resistance of in-situ synthesized Ti(C, N) ceramic reinforced Fe-based coating by laser cladding, Ceram. Int. 44 (2018) 22538–22548, https://doi.org/10.1016/j.ceramint.2018.09.025.
[39] T. Yu, Y. Zhao, J. Sun, Y. Chen, W. Qu, Process parameters optimization and mechanical properties of forming parts by direct laser fabrication of YCF101 alloy, J. Mater. Process. Technol. 262 (2018) 75–84, https://doi.org/10.1016/j.jmatprotec.2018.06.023.
[40] T. Wang, S. Dai, H. Liao, H. Zhu, Pores and the formation mechanisms of SLMed AlSi10Mg, Rapid Prototyp. J. 26 (2020) 1657–1664, https://doi.org/10.1108/RPJ-02-2020-0036.
[41] Z. Weng, A. Wang, X. Wu, Y. Wang, Z. Yang, Wear resistance of diode laser-clad Ni/WC composite coatings at different temperatures, Surf. Coating. Technol. 304 (2016) 283–292, https://doi.org/10.1016/j.surfcoat.2016.06.081.
[42] W.H. Jiang, R. Kovacevic, Laser deposited TiC/H13 tool steel composite coatings and their erosion resistance, J. Mater. Process. Technol. 186 (2007) 331–338, https://doi.org/10.1016/j.jmatprotec.2006.12.053.
[43] S. Sun, H. Fu, X. Ping, J. Lin, Y. Lei, W. Wu, J. Zhou, Reinforcing behavior and microstructure evolution of NbC in laser cladded Ni45 coating, Appl. Surf. Sci. 455 (2018) 160–170, https://doi.org/10.1016/j.apsusc.2018.05.199.
[44] W. Yuan, R. Li, Z. Chen, J. Gu, Y. Tian, A comparative study on microstructure and properties of traditional laser cladding and high-speed laser cladding of Ni45 alloy coatings, Surf. Coating. Technol. 405 (2021), 126582, https://doi.org/10.1016/j.surfcoat.2020.126582.
[45] C. Cui, Z. Guo, H. Wang, J. Hu, In situ TiC particles reinforced grey cast iron composite fabricated by laser cladding of Ni-Ti-C system, J. Mater. Process. Technol. 183 (2007) 380–385, https://doi.org/10.1016/j.jmatprotec.2006.10.031.
[46] Z. Liu, H. Qi, Effects of substrate crystallographic orientations on crystal growth and microstructure formation in laser powder deposition of nickel-based superalloy, Acta Mater. 87 (2015) 248–258, https://doi.org/10.1016/j.actamat.2014.12.046.
[47] Q. Wu, W. Li, N. Zhong, W. Gang, W. Haishan, Microstructure and wear behavior of laser cladding VC-$Cr_7C_3$ ceramic coating on steel substrate, Mater. Des. 49 (2013) 10–18, https://doi.org/10.1016/j.matdes.2013.01.067.
[48] Q. Sun, Z. Wang, J. Yang, Y. Liu, J. Liu, Z. Qiao, W. Liu, High-performance TiN reinforced Sialon matrix composites: a good combination of excellent toughness and tribological properties at a wide temperature range, Ceram. Int. 44 (2018) 17258–17265, https://doi.org/10.1016/j.ceramint.2018.06.185.
[49] Y. Zhao, T. Yu, C. Guan, J. Sun, X. Tan, Microstructure and friction coefficient of ceramic (TiC, TiN and $B_4C$) reinforced Ni-based coating by laser cladding, Ceram. Int. 45 (2019) 20824–20836, https://doi.org/10.1016/j.ceramint.2019.07.070.
[50] J. Lei, C. Shi, S. Zhou, Z. Gu, L.C. Zhang, Enhanced corrosion and wear resistance properties of carbon fiber reinforced Ni-based composite coating by laser cladding, Surf. Coating. Technol. 334 (2018) 274–285, https://doi.org/10.1016/j.surfcoat.2017.11.051.
[51] K.N. Xue, H.F. Lu, K.Y. Luo, C.Y. Cui, J.H. Yao, F. Xing, J.Z. Lu, Effects of Ni25 transitional layer on microstructural evolution and wear property of laser clad composite coating on H13 tool steel, Surf. Coating. Technol. 402 (2020), https://doi.org/10.1016/j.surfcoat.2020.126488.
[52] Z. Gan, G. Yu, X. He, S. Li, Numerical simulation of thermal behavior and multicomponent mass transfer in direct laser deposition of Co-base alloy on steel, Int. J. Heat Mass Tran. 104 (2017) 28–38, https://doi.org/10.1016/j.ijheatmasstransfer.2016.08.049.
[53] M.J. Bermingham, D.H. StJohn, J. Krynen, S. Tedman-Jones, M.S. Dargusch, Promoting the columnar to equiaxed transition and grain refinement of titanium alloys during additive manufacturing, Acta Mater. 168 (2019) 261–274, https://doi.org/10.1016/j.actamat.2019.02.020.
[54] Y. Zhao, T. Yu, J. Sun, L. Chen, Y. Chen, Effect of laser cladding on forming microhardness and tensile strength of YCF101 alloy powder in the different full lap joint modes, J. Alloys Compd. 820 (2020), 150230, https://doi.org/10.1016/j.jallcom.2019.04.046.
[55] W. Meng, W. Zhang, W. Zhang, X. Yin, B. Cui, Fabrication of steel-Inconel functionally graded materials by laser melting deposition integrating with laser synchronous preheating, Opt Laser. Technol. 131 (2020), 106451, https://doi.org/10.1016/j.optlastec.2020.106451.
[56] Y. Chen, F. Lu, K. Zhang, P. Nie, S.R. Elmi Hosseini, K. Feng, Z. Li, Dendritic microstructure and hot cracking of laser additive manufactured Inconel 718 under improved base cooling, J. Alloys Compd. 670 (2016) 312–321, https://doi.org/10.1016/j.jallcom.2016.01.250.
[57] L. Zhou, T. Yuan, R. Li, L. Li, Two ways of evaluating the wear property of Ti-13Nb-13Zr fabricated by selective laser melting, Mater. Lett. 242 (2019) 9–12, https://doi.org/10.1016/j.matlet.2019.01.015.

[58] Y. Guo, C. Li, M. Zeng, J. Wang, P. Deng, Y. Wang, In-situ TiC reinforced $CoCrCuFeNiSi_{0.2}$ high-entropy alloy coatings designed for enhanced wear performance by laser cladding, Mater. Chem. Phys. 242 (2020), 122522, https://doi.org/10.1016/j.matchemphys.2019.122522.

[59] F. Weng, H. Yu, C. Chen, J. Liu, L. Zhao, Microstructures and properties of TiN reinforced Co-based composite coatings modified with Y2O3 by laser cladding on Ti-6Al-4V alloy, J. Alloys Compd. 650 (2015) 178–184, https://doi.org/10.1016/j.jallcom.2015.07.295.

[60] K. Jia, T.E. Fischer, B. Gallois, Microstructure, hardness and toughness of nanostructured and conventional WC-Co composites, Nanostruct. Mater. 10 (1998) 875–891, https://doi.org/10.1016/S0965-9773(98)00123-8.

[61] G.F. Sun, X.T. Shen, Z.D. Wang, M.J. Zhan, S. Yao, R. Zhou, Z.H. Ni, Laser metal deposition as repair technology for 316L stainless steel: influence of feeding powder compositions on microstructure and mechanical properties, Opt Laser. Technol. 109 (2019) 71–83, https://doi.org/10.1016/j.optlastec.2018.07.051.

[62] N. Hutasoit, V. Luzin, A. Blicblau, W. Yan, M. Brandt, R. Cottam, Fatigue life of laser clad hardfacing alloys on AISI 4130 steel under rotary bending fatigue test, Int. J. Fatig. 72 (2015) 42–52, https://doi.org/10.1016/j.ijfatigue.2014.11.001.

[63] Z. Yang, L. Zhu, C. Ni, J. Ning, Investigation of surface topography formation mechanism based on abrasive-workpiece contact rate model in tangential ultrasonic vibration-assisted CBN grinding of $ZrO_2$ ceramics, Int. J. Mech. Sci. 155 (2019) 66–82, https://doi.org/10.1016/j.ijmecsci.2019.02.031.

[64] Z. Ma, Z. Wang, X. Wang, T. Yu, Effects of laser-assisted grinding on surface integrity of zirconia ceramic, Ceram. Int. 46 (2020) 921–929, https://doi.org/10.1016/j.ceramint.2019.09.051.

[65] H.N. Li, T.B. Yu, L. Da Zhu, W.S. Wang, Analytical modeling of ground surface topography in monocrystalline silicon grinding considering the ductile-regime effect, Arch. Civ. Mech. Eng. 17 (2017) 880–893, https://doi.org/10.1016/j.acme.2017.03.010.

[66] Z. Wang, T. Zhang, T. Yu, J. Zhao, Assessment and optimization of grinding process on AISI 1045 steel in terms of green manufacturing using orthogonal experimental design and grey relational analysis, J. Clean. Prod. 253 (2020), 119896, https://doi.org/10.1016/j.jclepro.2019.119896.